







## Penetration of Ultraviolet-B Radiation in Oligotrophic Regions of the Oceans During the Malaspina 2010 Expedition



### Key Points:

- During the expedition, we found the 5°–15°S region contained the most UV-B transparent waters
- Transparency to PAR was on average highest at ~20° latitude in both hemispheres
- $K_d$ (UV-B) was most strongly correlated with Chl-*a*, followed by  $a_{CDOM}(\lambda)$

S. Overmans<sup>1</sup> , C. M. Duarte<sup>1,2</sup> , C. Sobrino<sup>3</sup> , F. Iuculano<sup>4</sup> , X. A. Álvarez-Salgado<sup>5</sup> , and S. Agustí<sup>1</sup> 

<sup>1</sup>Red Sea Research Center (RSRC), King Abdullah University of Science and Technology (KAUST), Thuwal, Kingdom of Saudi Arabia, <sup>2</sup>Computational Biosciences Research Center (CBRC), King Abdullah University of Science and Technology (KAUST), Thuwal, Kingdom of Saudi Arabia, <sup>3</sup>Biological Oceanography Group, Department of Ecology and Animal Biology, University of Vigo, Vigo, Spain, <sup>4</sup>Global Change Research Group, Department of Oceanography and Global Change, Mediterranean Institute of Advanced Studies (IMEDEA), CSIC UIB, Esporles, Spain, <sup>5</sup>Organic Geochemistry Lab, Department of Oceanography, CSIC Instituto de Investigaciones Marinas, Vigo, Spain

### Supporting Information:

Supporting Information may be found in the online version of this article.

### Correspondence to:

S. Overmans,  
sebastian.overmans@kaust.edu.sa

### Citation:

Overmans, S., Duarte, C. M., Sobrino, C., Iuculano, F., Álvarez-Salgado, X. A., & Agustí, S. (2022). Penetration of ultraviolet-B radiation in oligotrophic regions of the oceans during the Malaspina 2010 Expedition. *Journal of Geophysical Research: Oceans*, 127, e2021JC017654. <https://doi.org/10.1029/2021JC017654>

Received 15 JUN 2021  
Accepted 29 APR 2022

### Author Contributions:

**Conceptualization:** S. Agustí  
**Data curation:** S. Overmans, S. Agustí  
**Formal analysis:** S. Overmans, C. M. Duarte, X. A. Álvarez-Salgado, S. Agustí  
**Funding acquisition:** C. M. Duarte  
**Investigation:** C. Sobrino, F. Iuculano  
**Methodology:** C. Sobrino, F. Iuculano, S. Agustí  
**Project Administration:** C. M. Duarte, S. Agustí  
**Resources:** C. M. Duarte, S. Agustí  
**Supervision:** C. M. Duarte, C. Sobrino, X. A. Álvarez-Salgado, S. Agustí  
**Validation:** S. Agustí

**Abstract** Few studies have investigated ultraviolet (UV) radiation in the open ocean besides its harmful effects on organisms and influence on biogeochemical processes. Here, we assessed UV attenuation, with particular focus on UV-B, across the (sub)tropical ocean during the Malaspina 2010 Circumnavigation. Vertical UV radiometer profiles together with Chl-*a* concentration, and UV absorption by CDOM ( $a_{CDOM}(\lambda)$ ) and by suspended particulate matter ( $a_p(\lambda)$ ) were measured at 117 stations. At photosynthetically active radiation (PAR) and across UV-A and UV-B wavelengths, the lowest downwelling attenuation coefficients ( $K_d$ ) during the expedition were recorded in ultra-oligotrophic regions at 5°–15°S (mean  $K_d$ (305 nm): 0.129 m<sup>-1</sup>, mean  $K_d$ (313 nm): 0.107 m<sup>-1</sup>) in the Indian and South Pacific Oceans. The waters here were comparatively more transparent than at 5°–15°N (mean  $K_d$ (305 nm): 0.239 m<sup>-1</sup>, mean  $K_d$ (313 nm): 0.181 m<sup>-1</sup>) where equatorial upwelling occurs.  $K_d$  was highest near the Costa Rica Dome ( $K_d$ (313 nm): 0.226 m<sup>-1</sup>) and at the confluence of the Benguela and Agulhas currents ( $K_d$ (313 nm): 0.251 m<sup>-1</sup>). The contribution of  $a_p(\lambda)$  toward nonwater absorption ( $a_{nw}(\lambda)$ ) was significantly lower at 305 nm than at 313 and 320 nm, suggesting the contribution of absorption by detritus and phytoplankton particles decreases compared with that of CDOM absorption as UV-B wavelength decreases. Both  $a_{CDOM}(\lambda)$  and  $a_p(\lambda)$  at UV-B wavelengths were lowest in the Indian Ocean whereas  $K_d$  was lowest in the South Pacific. This finding emphasizes that other factors besides absorption, such as scattering by reflective phytoplankton or inorganic particles, strongly influence UV-B attenuation in open ocean waters.

**Plain Language Summary** We assessed water transparency to UV-B radiation across the tropical and subtropical ocean as part of the Malaspina 2010 Expedition. UV-B radiometer profiles, Chlorophyll-*a*, and UV-B absorption by organic matter and suspended particles were measured at 117 stations. The most UV-B transparent waters were found in regions where nutrients are extremely low, particularly at 5°–15°S in the Indian and South Pacific Oceans. Here, ocean waters were considerably more transparent than 5°–15°N, which suggests that at a given depth southern hemisphere marine organisms experience higher UV-B exposure than their northern counterparts. The least UV-B transparent waters were near the Costa Rica Dome and at the confluence of the Benguela and Agulhas currents. UV-B absorption by organic matter and suspended particles, and Chl-*a* concentration were lowest in the Indian Ocean. The contribution of suspended particles toward nonwater absorption was significantly lower at 305 nm than at 313 and 320 nm, and higher in the clearest waters of the Indian Ocean than in the Subtropical South Pacific. Absorptions by organic matter and suspended particles were lowest in the Indian Ocean whereas UV-B attenuation was lowest in the South Pacific, which highlights the complex relationship between optical properties in the UV-B spectrum.

© 2022. The Authors.

This is an open access article under the terms of the [Creative Commons Attribution-NonCommercial-NoDerivs License](https://creativecommons.org/licenses/by/4.0/), which permits use and distribution in any medium, provided the original work is properly cited, the use is non-commercial and no modifications or adaptations are made.

## 1. Introduction

Solar radiation supplies photosynthetically active radiation (PAR: 400–700 nm), the energy source for oceanic photosynthesis, and ultraviolet radiation (UVR: 280–400 nm), which frequently results in adverse or inhibitory effects on biota and, therefore, represents a key stressor to marine biota (Häder et al., 2015; Llabres et al., 2013). More specifically, exposure to UV-B (280–320 nm) and UV-A (320–400 nm) has been shown to affect primary and secondary productivity, bacterial activity, the reproduction and development of organisms, and to alter

**Visualization:** S. Overmans, C. M. Duarte  
**Writing – original draft:** S. Overmans  
**Writing – review & editing:** S. Overmans, C. M. Duarte, C. Sobrino, F. Iuculano, X. A. Álvarez-Salgado, S. Agustí

community structure (García-Corral et al., 2017; Häder et al., 2015). High-energy UVR, and UV-B in particular, enables the photochemical formation and degradation of chromophoric dissolved organic matter (CDOM), thereby influencing its utilization by bacteria (Berto et al., 2016; Mopper & Kieber, 2002). However, the quantitative effects of UVR depend on the incident irradiances, which results from the solar radiation incident in the ocean surface and its attenuation in the water column. Previous studies suggested an asymmetry in stratospheric ozone and incident UV-B between the northern and southern hemispheres (Barnes et al., 2019; Weatherhead & Andersen, 2006), leading to higher incident UV-B at sea surface level in southern latitudes (Agusti et al., 2015). Hemispherical differences were also identified in the concentrations of UV-absorbing mycosporine-like amino acids (MAAs) in marine waters, with North Atlantic seston having higher MAA concentrations than Atlantic seston in southern latitudes (Fileman et al., 2017). Yet, several studies found that overall, marine biota from the southern hemisphere were more resistant to UV-B than their northern hemisphere counterparts (Agusti et al., 2015; Llabres et al., 2013), suggesting differences in UV-B induced stress between hemispheres in marine organisms.

Consequently, determining the propagation of UVR wavelengths in the marine environment is crucial in assessing the potential role of solar radiation on ocean ecosystem function and biogeochemical cycles.

The propagation of UVR in the ocean has received considerably less attention than PAR (Tedetti & Sempere, 2006), although assessments of UVR properties are available for enclosed seas (e.g., the Mediterranean Sea (Morel, Claustre et al., 2007; Organelli et al., 2014; Sempere et al., 2015) and the Red Sea (Dishon et al., 2012; Overmans & Agusti, 2019, 2020), or coastal systems and reefs (Downs et al., 2013; Kuwahara et al., 2010; Michael et al., 2012). For oceanic waters, UVR penetration has been reported in a few regions, including the Southern Ocean (Ban et al., 2007; Rasmus et al., 2004; Smith et al., 1992), the Northwest Pacific (Vasilkov et al., 2005), and the North Atlantic (Morel & Maritorena, 2001; Morrison & Nelson, 2004; Piazena et al., 2002; Smyth, 2011). The most transparent waters to UVR thus far reported are those in the South Pacific (Morel, Claustre et al., 2007; Tedetti et al., 2007), specifically in the hyper-oligotrophic and exceptionally transparent waters of the South Pacific gyre (Morel, Gentili et al., 2007; Morel et al., 2010; Smyth, 2011).

The extent to which UVR is attenuated in the water column is determined by its optical properties (Hargreaves, 2003), which in turn are governed by the optical properties of dissolved and particulate matter, and water itself. Measurements from exceptionally transparent oceanic waters found that pure seawater shows minimum light absorption in the blue-violet region (Lee et al., 2015; Morel, Gentili et al., 2007). CDOM, on the other hand, is the main contributor to UVR attenuation in natural waters (Helms et al., 2013; Kitidis et al., 2006) because its absorption increases exponentially from the PAR to the UV spectrum (Bricaud et al., 1981; Swan et al., 2009). Suspended particulate matter (SPM) also strongly contributes to the overall UVR attenuation, especially in coastal systems (Bricaud & Stramski, 1990; Mitchell et al., 2003; Nelson & Guarda, 1995), as these areas are receiving SPM from terrestrial sources, rivers, and coastal ecosystems. In the open ocean, the origin of both CDOM and SPM is predominantly autochthonous, generated by phytoplankton and other organisms (Andrew et al., 2013; Nelson et al., 2004; Twardowski & Donaghay, 2001). UVR absorption by particles has been reported to be low, representing ~20% of total biogenous, nonwater absorption ( $a_{nw}(\lambda)$ ) in the most transparent oceanic waters (Morel, Gentili et al., 2007). However, in situ UVR bio-optical data remain poorly explored (Tedetti & Sempere, 2006), including data from the oligotrophic subtropical gyres, which are characterized by low concentrations of Chl-*a*, CDOM and SPM (Bricaud et al., 2010; Iuculano et al., 2019), and are therefore the regions expected to have the most transparent waters to UVR.

Here, we report a globally coherent assessment of UVR penetration and its relationship to components of UVR attenuation in the Tropical and Subtropical Ocean, including the vast subtropical oligotrophic gyres. A further aim was to analyze possible differences in oceanic UVR attenuation between hemispheres. We do so by measuring UVR bio-optical properties and the main components of UVR attenuation in the tropical and subtropical Atlantic, Indian, and Pacific Oceans sampled along the Malaspina 2010 Circumnavigation Expedition (Duarte, 2015). Specifically, we present a global assessment of in situ UVR penetration, assess the relative contributions of the major biogeochemical drivers (i.e., CDOM and SPM) to the overall nonwater absorption ( $a_{nw}$ ) of UVR, and evaluate difference in UVR properties between northern and southern open ocean waters.

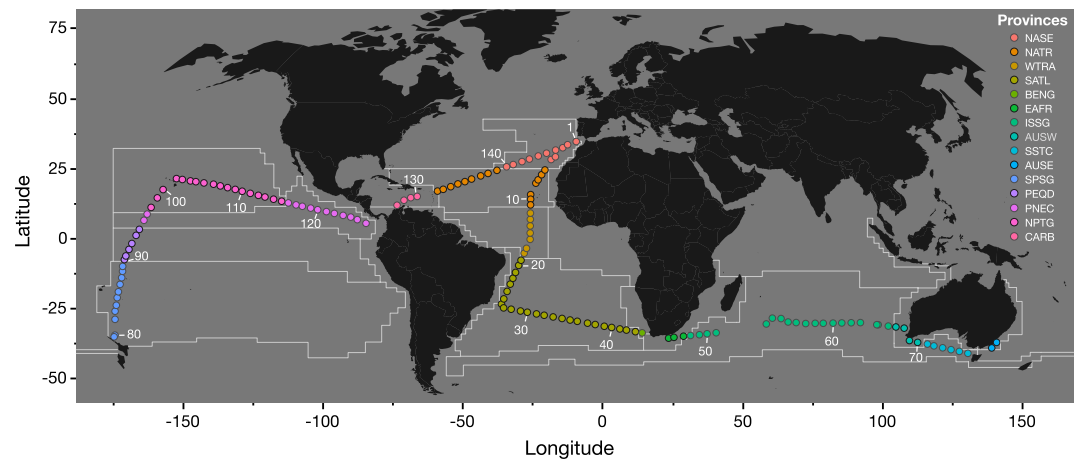


**Figure 1.** Cruise track of the Malaspina 2010 Circumnavigation Expedition, showing the locations and numbers of the 147 sampling stations. The colors of the circles indicate in which of the following Longhurst's biogeographic provinces a sampling station is located: NASE (North Atlantic Subtropical Gyral), NATR (North Atlantic Tropical Gyral), WTRA (Western Tropical Atlantic), SATL (South Atlantic Gyral), BENG (Benguela Current Coastal), EAFR (East Africa Coastal), ISSG (Indian South Subtropical Gyre), AUSW (Australia-Indonesia Coastal), SSTC (South Subtropical Convergence), AUSE (East Australian Coastal), SPSG (South Pacific Subtropical Gyre), PEQD (Pacific Equatorial Divergence), PNEC (North Pacific Equatorial Countercurrent), NPTG (North Pacific Tropical Gyre), and CARB (Caribbean).

## 2. Materials and Methods

### 2.1. Cruise Track and Division Into Longhurst's Provinces

The Malaspina 2010 Circumnavigation Expedition took place between 13 December 2010 and 14 July 2011 aboard the R/V *Hespérides*. The expedition included sampling stations in the Atlantic, Indian, and Pacific Oceans, covering a latitudinal range of 35.2°N to 40.5°S (Duarte, 2015; see Figure 1). A total of 147 stations were sampled and, based on their geographical location, grouped into 15 Longhurst's biogeographic provinces (Longhurst, 2010), following the classification of Catala et al. (2016). Six provinces were situated in the Atlantic Ocean, four in the Indian Ocean, and another five provinces in the Pacific Ocean. The locations of Longhurst's provinces and a description of their acronyms are shown in Figure 1.

### 2.2. Sample Collection and Environmental Parameters

A rosette sampler with 24 Niskin bottles (12 L volume each) was submerged at each station at approximately 10:00 (local time), and seawater was sampled from the surface down to the deep chlorophyll maximum (DCM). The percentage of PAR received at the DCM depth during the study corresponded to  $2.9 \pm 0.4\%$  (mean  $\pm$  SEM). For the quantification of Chl-*a*, and the absorptions by CDOM ( $a_{\text{CDOM}}(\lambda)$ ) and suspended particulate matter ( $a_p(\lambda)$ ), we analyzed samples from the surface (3 m) and two nominal depths according to the PAR profile, which included the depths where 50% ( $16.7 \pm 0.4$  m) and 20% ( $37.8 \pm 0.9$  m, mean  $\pm$  SEM) of surface PAR intensities were received (i.e.,  $Z_{50\%}(\text{PAR})$ ).  $Z_{20\%}(\text{PAR})$  was chosen as the lower limit because this depth corresponds to the spectroradiometer detection limit depth ( $\sim 40$  m) of the most rapidly attenuated UV wavelength (i.e., 305 nm). The rosette sampler was additionally equipped with a CTD probe Seabird 911 (Bellevue, WA, USA) and a Biospherical/Licor radiometer to continuously obtain vertical profiles of temperature, salinity, and PAR. The temperature and pressure sensors were calibrated at the SeaBird laboratory before the expedition. The salinity calibration was carried out daily onboard using a Guildline AUTOSAL model 8410B salinometer (Pérez-Hernández et al., 2012). Chl-*a* concentrations were determined fluorometrically from acetone extracts as described in Agustí et al. (2019).

### 2.3. UVR Spectroradiometer Measurements

Spectroradiometer profiles were recorded at 117 stations, while in the remaining 30 stations, rough waters prevented deployment of this instrument, which requires relatively calm conditions for safe operation. Specifically, we measured downwelling irradiance ( $E_d$ ) depth profiles at PAR (400–700 nm), and three UV-B (305,

313, and 320 nm) and UV-A (340, 380, and 395 nm) narrow bands (10 nm FWHM standard) with a calibrated PRR 800 Profiling Reflectance Radiometer (Biospherical Instruments, San Diego, USA). The radiometer was equipped with a pressure sensor, and irradiances were continuously recorded (5 Hz) during the profiling. The vessel was maneuvered relative to the sun to ensure the hull did not cast a shadow over the instrument. All profiles were recorded around midday (11:00–13:00 local time) to minimize differences in solar angle between measurements. Some profiles were repeated at the station if weather conditions changed during the measurement. Only profiles acquired during stable sky conditions are considered here for the calculation of downwelling attenuation coefficients.

#### 2.4. Absorption by CDOM

At each station, seawater samples were taken from the surface (~3 m) and the 50% and 20% PAR depths for the quantitative analysis of CDOM, as described in Iuculano et al. (2019). Briefly, 125 mL of each seawater sample was transferred into acid-washed bottles and stored in darkness at 4°C until further processing. Within 2–3 hr of collection, 50 mL aliquots were filtered through a PTFE filter (0.2 μm pore size) to remove particulate matter. The first 20 mL were used to preflush the filter and subsequently discarded, while the absorption measurements were performed on the remaining 30 mL. Absorption coefficients of CDOM ( $a_{\text{CDOM}}$ ) were determined from the UV-visible absorption spectra of CDOM (250–750 nm) measured at 1-nm resolution in 10-cm path length quartz cuvettes, using a dual-beam Perkin Elmer lambda 850 spectrophotometer. The sample spectra were compared against the spectrum of fresh Milli-Q water as a reference. The mean absorbance between 600 and 750 nm was subtracted from all measurements to correct for differences in the refractive index, residual scattering, and light attenuation due to sources other than CDOM. The CDOM absorption coefficients ( $a_{\text{CDOM}}(\lambda)$ , in  $\text{m}^{-1}$ ) were calculated as shown in

$$a_{\text{CDOM}}(\lambda) = 2.303 \times \frac{[OD_{\text{CDOM}}(\lambda) - OD_{\text{CDOM}}(600 - 750 \text{ nm})]}{l} \quad (1)$$

where 2.303 is the factor used to convert base-10 logarithms to base- $e$  logarithms,  $OD_{\text{CDOM}}(\lambda)$  is the optical density or absorbance at wavelength  $\lambda$ ,  $OD_{\text{CDOM}}(600-750 \text{ nm})$  is the average optical density between 600 and 750 nm, and  $l$  is the path length of the cuvette (0.1 m). We focused our  $a_{\text{CDOM}}$  analysis on the UV-B wavelengths recorded by the profiling UV-spectroradiometer used (305, 313, and 320 nm). These three wavelengths cover most of the UV-B that reaches the Earth's surface, given that the atmosphere is not transparent to radiation <295 nm (Fichot & Benner, 2011).

#### 2.5. Absorption by Suspended Particulate Matter

UVR absorption coefficients of suspended particulate matter ( $a_p(\lambda)$ ) were determined spectrophotometrically using the filter-pad method (Mitchell et al., 2003). Seawater samples (1.0–3.0 L) collected from 3 m and the 50% and 20% PAR depths were filtered onto Whatman® glass microfiber filters (25-mm diameter, grade GF/F), which have a particle retention comparable to the 0.2 μm PTFE filter used for CDOM (Estrada et al., 2016). The filters were maintained wet and kept in the dark (<1 hr) until the optical density was measured. Optical densities of total particulate matter ( $OD_{p(\lambda)}$ ) were between 280 and 750 nm at a spectral resolution of 1 nm using the same dual-beam spectrophotometer as for  $a_{\text{CDOM}}(\lambda)$ , and a clean, water-saturated Whatman GF/F filter as a blank. The wet sample and the blank filter were placed in quartz slides in front of the photomultiplier and the blank photomultiplier, respectively. For each spectrum, the OD at 750 nm was used as a null-absorption reference. All spectra were converted into  $a_p(\lambda)$ ; in  $\text{m}^{-1}$ ) and corrected for the path length amplification effect according to Bricaud and Stramski (1990)

$$a_p(\lambda) = 2.303 \times OD_p(\lambda) \times s / [V \times \beta(\lambda)] \quad (2)$$

where 2.303 is the factor used to convert base-10 logarithms to base- $e$  logarithms,  $OD_p(\lambda)$  is the optical density at wavelength  $\lambda$ ,  $s$  is the clearance area of the filter (in  $\text{m}^{-2}$ ),  $V$  is the volume of filtered water (in  $\text{m}^{-3}$ ), and  $\beta(\lambda)$  refers to the path length amplification factor (Mitchell & Kiefer, 1984).

## 2.6. Data Analysis

### 2.6.1. UVR Attenuation Coefficients ( $K_d$ )

A visual quality check was performed on the spectroradiometer profile data to remove any apparent outliers or erroneous irradiance values. Irradiance versus depth profiles from the spectroradiometer casts were used to calculate downwelling diffuse attenuation coefficients,  $K_d(\lambda)$ , as the slope of a linear regression of the natural logarithm of  $F_\lambda$  (fraction of spectral irradiance at wavelength  $\lambda$ ) against  $z$  (depth, in m) as shown in Equation 3 (logarithmic form of Beer's law)

$$\ln F_\lambda = -K_d(\lambda) \times z \quad (3)$$

The fitting process was highly robust, with coefficients of determination ( $R^2$ ) > 0.99.  $K_d(\lambda)$  of the UVR channels (305, 313, 320, 340, 380, and 395 nm) was calculated from the surface down to the detection limit (~40 m) of the most rapidly attenuated wavelength (i.e., 305 nm), and for PAR down to its approximate detection limit of 100 m.

### 2.6.2. Ten Percent Attenuation Depth ( $Z_{10\%}$ )

For UVR wavelengths (305, 313, 320, 340, 380, and 395 nm), and the integrated PAR spectrum (400–700 nm), we calculated the 10% attenuation depth ( $Z_{10\%}$ ), which is defined as the depth where irradiance is reduced to 10% of the surface value.  $Z_{10\%}$  was calculated using  $K_d$ , as shown in

$$Z_{10\%} = \frac{\ln(10)}{K_d} \quad (4)$$

The 10% attenuation depth is especially relevant in terms of the PAR spectrum because it represents the midpoint of the euphotic zone (Kirk, 1994; Lee et al., 2007). In the context of UV,  $Z_{10\%}$  is defined as the biologically effective optical depth of UVR (Kuwahara et al., 2010), where the irradiance may be damaging to marine organisms.

### 2.6.3. Statistical Analysis

We performed a series of Kruskal-Wallis tests and subsequent Dunn's pairwise comparison post hoc tests, i.e., one Kruskal-Wallis test for each UVR wavelength and PAR, to identify significant differences between the mean  $K_d(\lambda)$  of Longhurst's provinces. The province BENG was excluded from this analysis since only one station was sampled here, and accompanying  $a_{\text{CDOM}}$  and  $a_p$  data were not available. Additional Kruskal-Wallis tests and Dunn's tests were performed to determine whether  $a_{\text{CDOM}}$ ,  $a_p$ , and the contribution of  $a_p$  toward  $a_{\text{nw}}$  (in %) differed significantly at 305, 313, and 320 nm and between Longhurst's provinces. Differences were considered statistically significant at a level of  $p < 0.05$ . Furthermore, we calculated Pearson's correlation coefficients ( $r$ ) to determine the strength of association between the variables temperature, Chl-*a* concentration,  $K_d(\text{PAR})$ ,  $a_{\text{CDOM}}(\lambda)$ ,  $a_p(\lambda)$ , and  $K_d(\lambda)$  at wavelengths ( $\lambda$ ) 305, 313, and 320 nm. For the correlation analysis, we used depth-weighted values of Chl-*a*,  $a_{\text{CDOM}}(\lambda)$ , and  $a_p(\lambda)$ , which were calculated as follows:

$$\text{Depth-weighted } x = 0.5 \times [(x_1 + x_2) \times (Z_2 - Z_1) + (x_2 + x_3) \times (Z_3 - Z_2)] / (Z_3 - Z_1) \quad (5)$$

where  $x$  refers to either Chl-*a*,  $a_{\text{CDOM}}(\lambda)$ , or  $a_p(\lambda)$ .  $Z$  denotes depth (in m), while 1, 2, and 3 refer to the corresponding values at the surface, and the 50% and 20% PAR depths, respectively.

Lastly, two multiple linear regressions were performed per UV-B wavelength to predict  $K_d(\lambda)$  based on depth-weighted values of (1)  $a_{\text{CDOM}}(\lambda)$  and  $a_p(\lambda)$  and (2)  $a_{\text{CDOM}}(\lambda)$ ,  $a_p(\lambda)$ , and Chl-*a* concentration. Chl-*a* was additionally tested as an independent variable due to its high correlation with absorption and backscattering in Case-1 waters. We used the ANOVA function (stats) in the software packages R and R studio (version 2021.09.0) to compare between the two nested models. The remaining data were analyzed and visualized using either JMP Pro 15.1.0 (SAS Institute Inc., Cary, NC, USA) or GraphPad Prism 8.4.3 (GraphPad Software Inc., CA, USA).

## 3. Results

### 3.1. Biogeochemical Properties

Water temperature averaged  $24.6 \pm 0.1^\circ\text{C}$  (mean  $\pm$  SEM) between the surface (3 m) and the 20% PAR depth ( $37.8 \pm 0.9$  m, mean  $\pm$  SEM; Table 1), with temperatures ranging from 16.0 to 29.3°C at the surface, 15.7–29.3°C

**Table 1**

Summary of the Basic Oceanographic Parameters Temperature (in °C) and Chl-*a* Concentration (in mg m<sup>-3</sup>), as Well as  $a_{\text{CDOM}}$  and  $a_p$  (in m<sup>-1</sup>), Measured Between the Surface and the 20% PAR Depth in 15 Longhurst's Provinces That Were Visited as Part of the Malaspina 2010 Circumnavigation

Province	Temp	Chl- <i>a</i>	$a_{\text{CDOM}}$ (305 nm)	$a_{\text{CDOM}}$ (313 nm)	$a_{\text{CDOM}}$ (320 nm)	$a_p$ (305 nm)	$a_p$ (313 nm)	$a_p$ (320 nm)
AUSE	21.4 ± 0.1	0.317 ± 0.011	0.286 ± 0.071	0.239 ± 0.070	0.222 ± 0.052	0.015 ± 0.001	0.013 ± 0.001	0.012 ± 0.001
AUSW	21.9 ± 0.6	0.121 ± 0.006	0.193 ± 0.025	0.147 ± 0.023	0.148 ± 0.021	0.015 ± 0.002	0.014 ± 0.001	0.012 ± 0.001
BENG	20.5 ± 0.1	0.236 ± 0.015	NA	NA	NA	NA	NA	NA
CARB	28.8 ± 0.1	0.140 ± 0.011	0.334 ± 0.033	0.277 ± 0.030	0.252 ± 0.027	0.024 ± 0.002	0.024 ± 0.002	0.023 ± 0.002
EAFR	24.4 ± 0.5	0.205 ± 0.059	0.231 ± 0.018	0.181 ± 0.015	0.168 ± 0.014	0.016 ± 0.002	0.014 ± 0.002	0.013 ± 0.002
ISSG	23.3 ± 0.2	0.079 ± 0.006	0.139 ± 0.005	0.109 ± 0.005	0.101 ± 0.005	0.011 ± 0.000	0.010 ± 0.000	0.008 ± 0.000
NASE	21.6 ± 0.2	0.089 ± 0.009	0.250 ± 0.017	0.204 ± 0.016	0.180 ± 0.015	0.013 ± 0.001	0.012 ± 0.001	0.011 ± 0.001
NATR	26.3 ± 0.2	0.128 ± 0.012	0.222 ± 0.015	0.173 ± 0.012	0.146 ± 0.011	0.015 ± 0.001	0.014 ± 0.001	0.013 ± 0.001
NPTG	23.9 ± 0.2	0.179 ± 0.013	0.284 ± 0.018	0.240 ± 0.017	0.220 ± 0.016	0.021 ± 0.001	0.019 ± 0.001	0.016 ± 0.001
PEQD	27.9 ± 0.1	0.240 ± 0.018	0.289 ± 0.022	0.242 ± 0.021	0.243 ± 0.019	0.023 ± 0.002	0.020 ± 0.002	0.020 ± 0.002
PNEC	27.2 ± 0.5	0.363 ± 0.026	0.427 ± 0.021	0.360 ± 0.020	0.330 ± 0.018	0.027 ± 0.002	0.024 ± 0.002	0.022 ± 0.001
SATL	24.4 ± 0.3	0.082 ± 0.006	0.216 ± 0.013	0.169 ± 0.012	0.161 ± 0.011	0.015 ± 0.001	0.013 ± 0.001	0.012 ± 0.001
SPSG	27.2 ± 0.5	0.121 ± 0.007	0.329 ± 0.023	0.278 ± 0.022	0.267 ± 0.024	0.025 ± 0.001	0.022 ± 0.001	0.022 ± 0.001
SSTC	17.1 ± 0.2	0.247 ± 0.025	0.288 ± 0.033	0.229 ± 0.029	0.236 ± 0.030	0.018 ± 0.002	0.017 ± 0.002	0.015 ± 0.002
WTRA	26.9 ± 0.4	0.299 ± 0.037	0.191 ± 0.005	0.146 ± 0.005	0.127 ± 0.005	0.016 ± 0.001	0.015 ± 0.001	0.014 ± 0.001
Overall	24.6 ± 0.1	0.162 ± 0.006	0.252 ± 0.006	0.205 ± 0.006	0.190 ± 0.005	0.018 ± 0.000	0.016 ± 0.000	0.015 ± 0.000

Note. Values are means ± SEM.

at the 50% PAR depth, and 15.3–29.3°C at the 20% PAR depth. The lowest mean temperature (17.1 ± 0.2°C) was recorded in the Longhurst's province SSTC, situated along the Great Australian Bight, while the highest mean temperature (28.8 ± 0.1°C) was measured in the Caribbean province CARB.

Chl-*a* concentration between the surface and the 20% PAR depth was on average 0.162 ± 0.006 mg m<sup>-3</sup> (mean ± SEM; Table 1), with concentrations ranging from 0.034 to 0.693 mg m<sup>-3</sup> (surface), 0.034–0.496 mg m<sup>-3</sup> (50% PAR depth), and 0.041–1.083 mg m<sup>-3</sup> (20% PAR depth). The lowest mean Chl-*a* (0.079 ± 0.006 mg m<sup>-3</sup>) was measured in the Indian Ocean province ISSG, while Chl-*a* was on average highest (0.363 ± 0.026 mg m<sup>-3</sup>) at PNEC off the Pacific coast of Costa Rica (Table 1).

### 3.2. CDOM Absorption Coefficients ( $a_{\text{CDOM}}$ )

In the upper photic layer (from surface to 20% PAR depth),  $a_{\text{CDOM}}(\lambda)$  ranged from 0.066 to 0.707 m<sup>-1</sup>, 0.032 to 0.637 m<sup>-1</sup>, and 0.052 to 0.657 m<sup>-1</sup> at wavelengths 305, 313, and 320 nm, respectively (Figure 2; Figure S1 in Supporting Information S1). At each UV-B wavelength, the lowest  $a_{\text{CDOM}}(\lambda)$ ; mean ± SEM) were measured in the province ISSG (305 nm: 0.139 ± 0.005 m<sup>-1</sup>; 313 nm: 0.109 ± 0.005 m<sup>-1</sup>; 320 nm: 0.101 ± 0.005 m<sup>-1</sup>), while the highest mean values were found in PNEC (305 nm: 0.427 ± 0.021 m<sup>-1</sup>; 313 nm: 0.360 ± 0.020 m<sup>-1</sup>; 320 nm: 0.330 ± 0.018 m<sup>-1</sup>; Table 1). Overall,  $a_{\text{CDOM}}(\lambda)$  was significantly different between Longhurst's provinces at 305 nm ( $\chi^2 = 167.39$ ,  $df = 13$ ,  $p < 0.0001$ ), 313 nm ( $\chi^2 = 159.87$ ,  $df = 13$ ,  $p < 0.0001$ ), and 320 nm ( $\chi^2 = 163.75$ ,  $df = 13$ ,  $p < 0.0001$ ). Pairwise comparisons indicated that at each of those wavelengths, the  $a_{\text{CDOM}}(\lambda)$  measured in ISSG were significantly lower ( $p < 0.01$ ) compared to most provinces, except AUSE, AUSW, EAFR, and WTRA (Figure S2 in Supporting Information S1). Also,  $a_{\text{CDOM}}(\lambda)$  was significantly lower ( $p < 0.01$ ) at ISSG than at NATR at wavelengths 305 and 313 nm. Across UV-B wavelengths, the North Pacific province PNEC had a significantly higher ( $p < 0.01$ )  $a_{\text{CDOM}}(\lambda)$  compared to AUSW, NASE, NATR, SATL, and WTRA. Lastly, SATL had a significantly lower  $a_{\text{CDOM}}(305 \text{ nm})$  than CARB ( $p < 0.05$ ) and SPSG ( $p < 0.01$ ), a lower  $a_{\text{CDOM}}(313 \text{ nm})$  compared to CARB ( $p < 0.05$ ), NPTG ( $p < 0.05$ ), and SPSG ( $p < 0.001$ ), and a lower  $a_{\text{CDOM}}(320 \text{ nm})$  than PEQD ( $p < 0.05$ ) and SPSG ( $p < 0.01$ ).

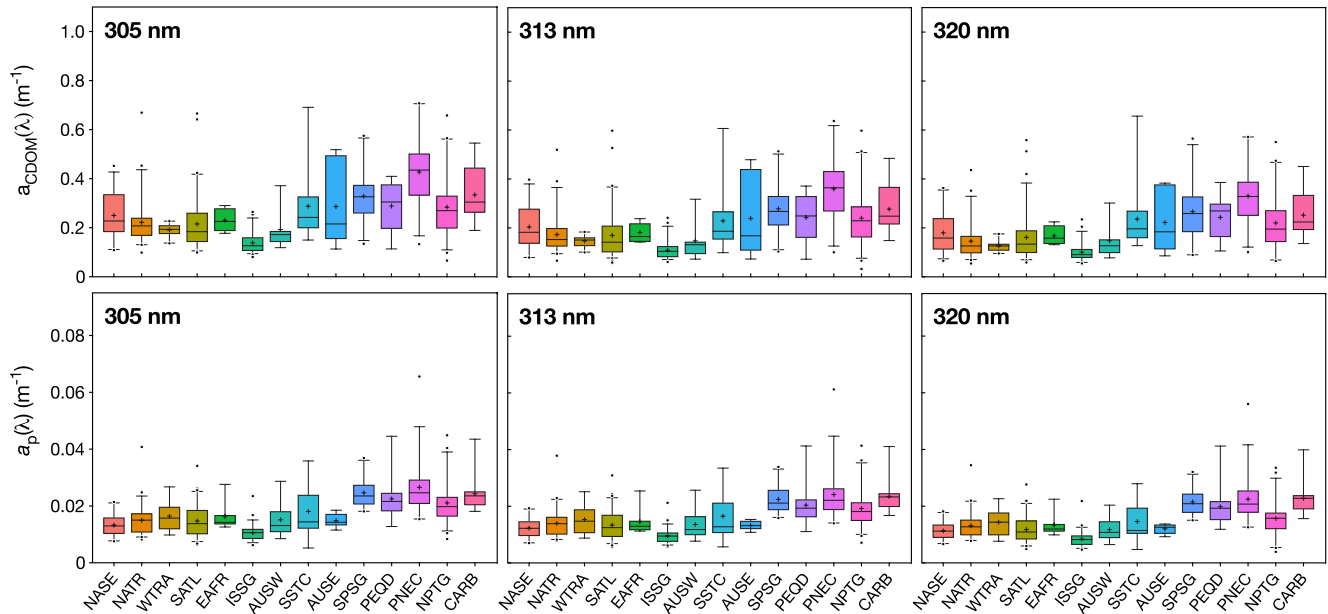


**Figure 2.** Chromophoric dissolved organic matter (CDOM) absorption coefficients ( $a_{CDOM}$ , in  $m^{-1}$ ) (upper panels) and particulate absorption coefficients ( $a_p$ , in  $m^{-1}$ ) (lower panels) at the three UV-B wavelengths 305 nm (left panels), 313 nm (middle panels), and 320 nm (right panels) measured in 14 Longhurst's biogeographical provinces (see Figure 1 for legend key) during the Malaspina 2010 Expedition. The horizontal line in plots shows the median, crosses represent the mean, while whiskers indicate the upper and lower 95% confidence intervals.

### 3.3. Particulate Absorption Coefficients ( $a_p$ )

Overall, we found that the shape of  $a_p$  spectra varied considerably across Longhurst's provinces (Figure 3). For example, we found that some provinces (e.g., ISSG, AUSW, AUSE) exhibited spectra that were exceptionally homogenous in shape and magnitude, with little differences between stations. In contrast, some provinces showed considerable differences between individual spectra (e.g., provinces WTRA, SSTC, PEQD, PNEC, and NPTG).

The absorption coefficients of suspended particulate matter ( $a_p(\lambda)$ ) at wavelengths 305, 313, and 320 nm ranged from 0.005 to 0.066  $m^{-1}$ , 0.006 to 0.061  $m^{-1}$ , and 0.004 to 0.056  $m^{-1}$ , respectively (Figure 2; Figure S3 in Supporting Information S1).

Likewise to  $a_{CDOM}(\lambda)$ , we measured the lowest mean  $a_p(\lambda)$  at UV-B wavelengths in ISSG (305 nm:  $0.011 \pm 0.0004 m^{-1}$ ; 313 nm:  $0.010 \pm 0.0003 m^{-1}$ ; 320 nm:  $0.008 \pm 0.0004 m^{-1}$ ; Table 1). The location of the highest mean  $a_p(\lambda)$ , on the other hand, was wavelength dependent, with  $a_p(305 nm)$  and  $a_p(313 nm)$  being highest in PNEC (305 nm:  $0.027 \pm 0.002 m^{-1}$ ; 313 nm:  $0.024 \pm 0.002 m^{-1}$ ), and  $a_p(320 nm)$  showing the highest average in the province CARB ( $0.023 \pm 0.002 m^{-1}$ ). Comparing  $a_p(\lambda)$  between provinces revealed a significant difference overall at wavelengths 305 nm ( $\chi^2 = 196.65$ ,  $df = 13$ ,  $p < 0.0001$ ), 313 nm ( $\chi^2 = 193.24$ ,  $df = 13$ ,  $p < 0.0001$ ), and 320 nm ( $\chi^2 = 191.74$ ,  $df = 13$ ,  $p < 0.0001$ ). Pairwise comparisons between provinces found that, at each UV-B wavelength, ISSG had a significantly lower  $a_p(\lambda)$ ;  $p < 0.05$ ) than most provinces, except for AUSE, AUSW, EAFR, and NASE (Figure S2 in Supporting Information S1). The province PNEC had significantly higher  $a_p(\lambda)$  compared to provinces AUSW, NASE, NATR, SATL, and SSTC at 305, 313, and 320 nm. PNEC also had significantly higher  $a_p(305 nm)$  and  $a_p(313 nm)$  than WTRA. Across UV-B wavelengths, the province SATL was characterized by  $a_p(\lambda)$  that were significantly lower than at CARB, PEQD, and SPSG. NASE and NATR had  $a_p(\lambda)$  values that were significantly lower than those found in provinces CARB, PEQD, and SPSG at 305, 313, and 320 nm, and lower than those in NPTG at 305 and 313 nm.

### 3.4. UVR and PAR Attenuation Coefficients ( $K_d$ ) and $Z_{n\%}$

The downwelling diffuse attenuation coefficients ( $K_d(\lambda)$ ) at 305, 313, and 320 nm ranged from 0.079 to 0.478  $m^{-1}$ , 0.074 to 0.387  $m^{-1}$ , and 0.074 to 0.370  $m^{-1}$ , respectively (Figure 4, Figure S4 in Supporting Information S1).

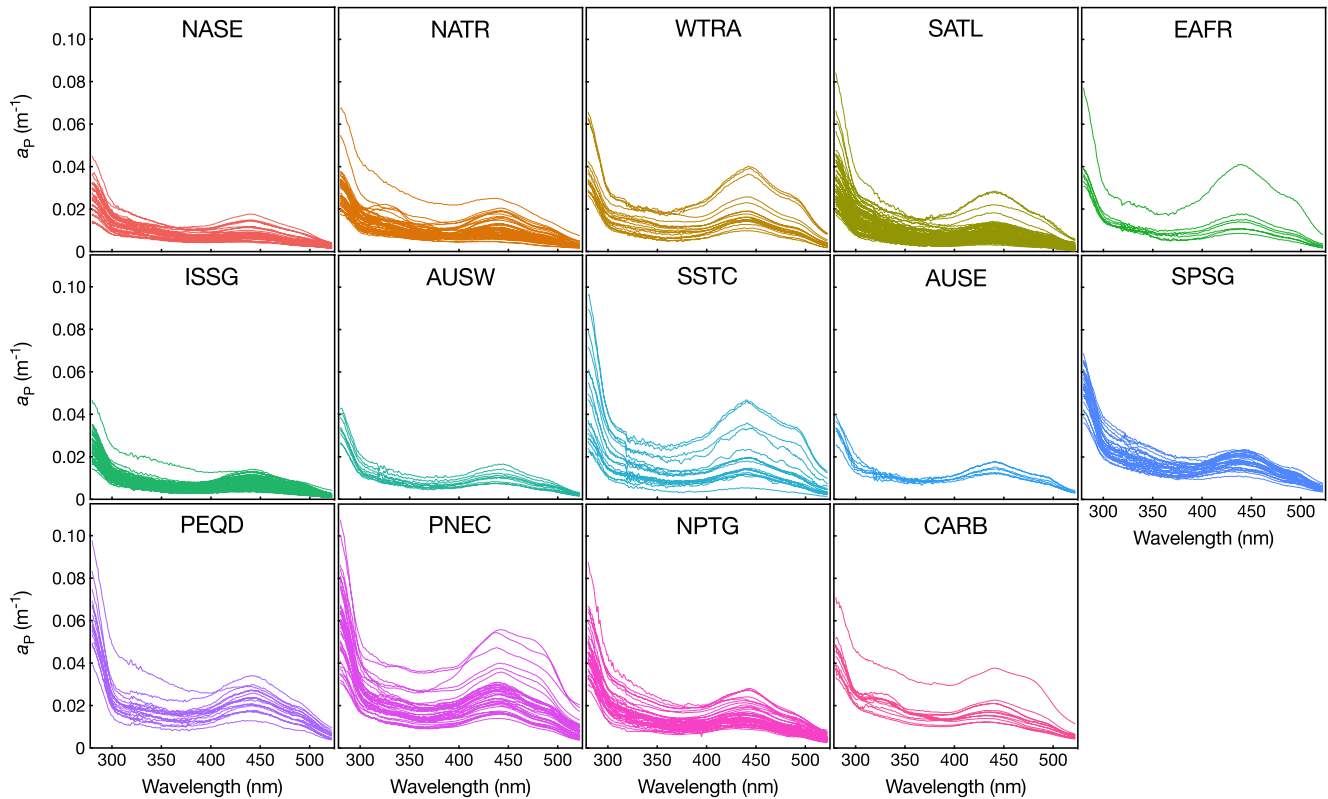


**Figure 3.** Wavelength spectra of particulate absorption coefficients ( $a_p$ , in  $\text{m}^{-1}$ ) determined between the surface and 20% photosynthetically active radiation (PAR) depth at 14 Longhurst's biogeographical provinces (see Figure 1 for legend key) during the Malaspina 2010 Expedition.

For UV-A wavelengths,  $K_d(\lambda)$  varied from 0.041 to 0.260  $\text{m}^{-1}$  (340 nm), 0.024 to 0.164  $\text{m}^{-1}$  (380 nm), and 0.017 to 0.147  $\text{m}^{-1}$  (395 nm; Figure 4, Figure S5 in Supporting Information S1), and from 0.021 to 0.117  $\text{m}^{-1}$  for the integrated PAR spectrum (Figure 4, Figure S6 in Supporting Information S1). Of the 10 most UV-transparent waters identified during the expedition, two were located in province ISSG, two in NPTG, and six in SPSG (Table 2). Across Longhurst's provinces, SPSG had the lowest  $K_d(\lambda)$ ; mean  $\pm$  SEM) at wavelengths 305 ( $0.108 \pm 0.009 \text{ m}^{-1}$ ), 313 ( $0.098 \pm 0.004 \text{ m}^{-1}$ ), 320 ( $0.100 \pm 0.005 \text{ m}^{-1}$ ), and 340 nm ( $0.062 \pm 0.004 \text{ m}^{-1}$ ; Table 3). At longer wavelengths, SATL exhibited the lowest mean  $K_d(\lambda)$ , i.e., at 380 ( $0.044 \pm 0.003 \text{ m}^{-1}$ ) and 395 nm ( $0.036 \pm 0.002 \text{ m}^{-1}$ ) and PAR ( $0.036 \pm 0.002 \text{ m}^{-1}$ ). The highest mean  $K_d(\lambda)$  was observed in province PNEC at wavelengths 305 ( $0.293 \pm 0.034 \text{ m}^{-1}$ ), 313 ( $0.226 \pm 0.027 \text{ m}^{-1}$ ), 320 ( $0.214 \pm 0.026 \text{ m}^{-1}$ ), 340 ( $0.150 \pm 0.018 \text{ m}^{-1}$ ), 380 ( $0.104 \pm 0.011 \text{ m}^{-1}$ ), and 395 nm ( $0.093 \pm 0.010 \text{ m}^{-1}$ ), whereas  $K_d(\text{PAR})$  was highest in EAFR ( $0.081 \pm 0.036 \text{ m}^{-1}$ ).

Comparison of  $K_d(\lambda)$  between Longhurst's provinces revealed an overall significant difference ( $df = 13$ ,  $p < 0.0001$ ) at 305 nm ( $\chi^2 = 61.72$ ), 313 nm ( $\chi^2 = 58.44$ ), 320 nm ( $\chi^2 = 54.41$ ), 340 nm ( $\chi^2 = 51.86$ ), 380 nm ( $\chi^2 = 49.76$ ), and 395 nm ( $\chi^2 = 48.64$ ), and PAR ( $\chi^2 = 53.55$ ). Pairwise comparisons found that at each UVR wavelength and PAR, PNEC had a significantly higher  $K_d(\lambda)$  than SATL and SPSG (Figure S7 in Supporting Information S1). PNEC also had a significantly higher  $K_d(\lambda)$  than ISSG at PAR and all UVR wavelengths except 380 nm, as well as a higher  $K_d(\lambda)$  than NPTG at PAR and wavelengths 320, 340, 380, and 395 nm. SPSG had a significantly lower  $K_d(\lambda)$  than NATR at 305 nm, SSTC at 305 nm, and WTRA at 305, 313, and 340 nm ( $p < 0.01$ ). SATL had significantly lower  $K_d(395 \text{ nm})$  and  $K_d(\text{PAR})$ ;  $p < 0.01$ ) than WTRA.

$K_d(305)$  and  $K_d(313)$  were lowest in the  $5^\circ$ – $15^\circ\text{S}$  latitudinal band, where the most UV-transparent waters in the expedition were found (Figure 5). The highest  $K_d(305)$ ,  $K_d(313)$ , and  $K_d(\text{PAR})$  were obtained between the equator and  $10^\circ\text{N}$ , corresponding to the equatorial upwelling region. Based on UV-B  $K_d$  values, we determined that the 10% attenuation depth ( $Z_{10\%}$ ) of 305, 313, and 320 nm ranged from 4.8 to 29.2 m (mean: 14.1 m), 5.9–31.1 m



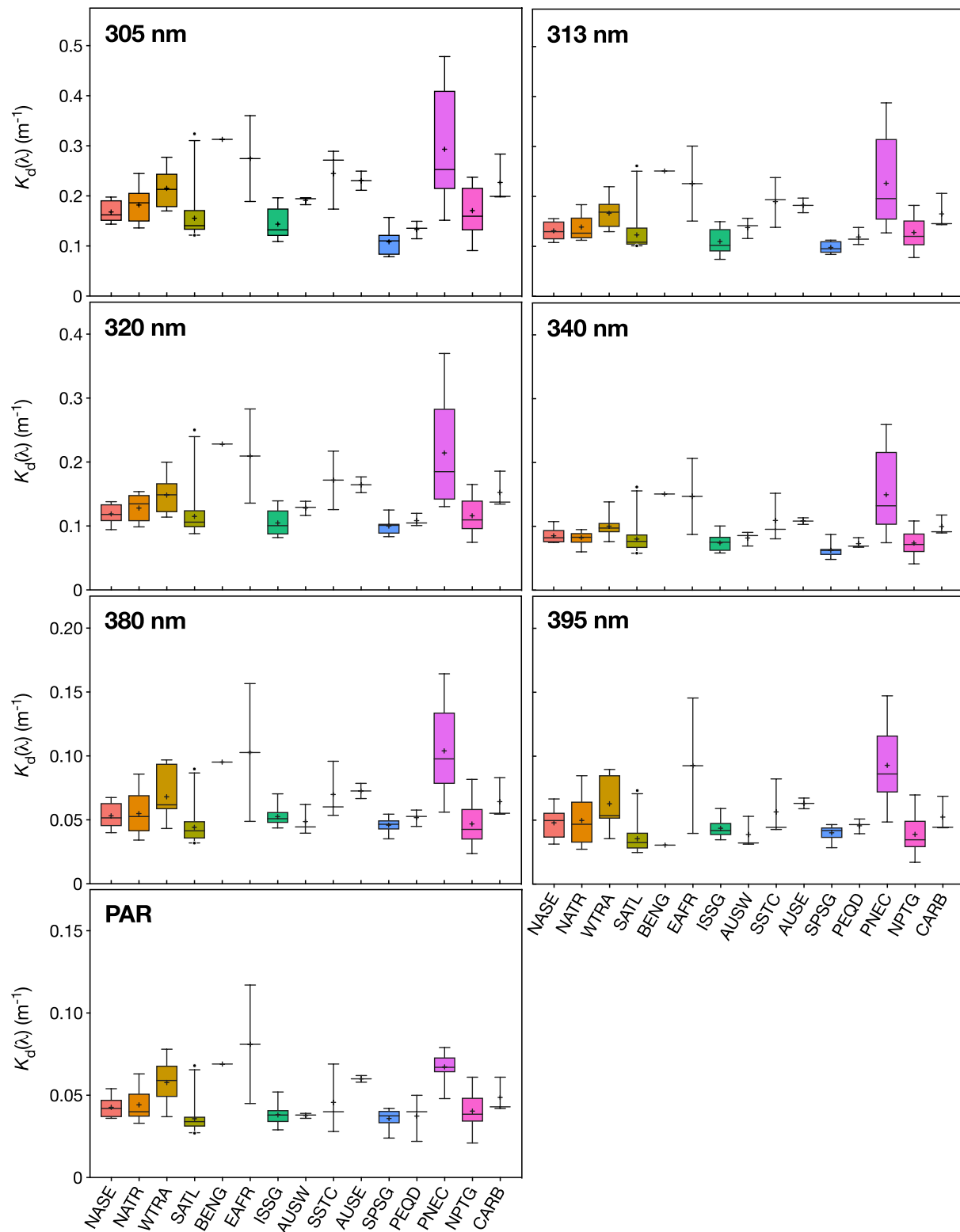


**Figure 4.** Downwelling diffuse attenuation coefficients ( $K_d$ , in  $m^{-1}$ ) of the ultraviolet radiation (UVR) wavelengths 305, 313, 320, 340, 380, and 395 nm, and the integrated photosynthetically active radiation (PAR) spectrum shown for 15 Longhurst's provinces that were sampled as part of the Malaspina 2010 Expedition. The horizontal line in plots shows the median, crosses represent the mean, while whiskers indicate the upper and lower 95% confidence intervals.

**Table 2**

Location and  $K_d(\lambda)$  of the 10 Stations With the Most UV-Transparent Waters, Based on Downwelling Diffuse Attenuation Coefficients ( $K_d$ , in  $m^{-1}$ ) Measured During the Malaspina 2010 Expedition

Station	Province	Latitude	Longitude	$K_d$ (305 nm)	$K_d$ (313 nm)	$K_d$ (320 nm)	$K_d$ (340 nm)	$K_d$ (380 nm)	$K_d$ (395 nm)	$K_d$ (PAR)
56	ISSG	-29.561	72.444	0.109	0.074	0.083	0.058	0.051	0.041	0.036
60	ISSG	-29.749	86.257	0.113	0.088	0.086	0.060	0.045	0.035	0.029
84	SPSG	-20.661	-176.920	0.113	0.113	0.101	0.087	0.050	0.041	0.033
85	SPSG	-18.561	-175.823	0.108	0.091	0.102	0.048	0.035	0.028	0.033
86	SPSG	-15.903	-174.487	0.093	0.084	0.101	0.065	0.055	0.047	0.041
87	SPSG	-13.531	-173.372	0.079	0.100	0.085	0.063	0.044	0.043	0.042
88	SPSG	-11.242	-172.630	0.079	0.086	0.083	0.055	0.046	0.045	0.039
89	SPSG	-9.474	-172.298	0.114	0.090	0.104	0.062	0.042	0.035	0.036
99	NPTG	14.997	-160.816	0.114	0.093	0.095	0.057	0.032	0.026	0.032
100	NPTG	17.973	-159.435	0.091	0.078	0.074	0.041	0.033	0.028	0.030

(mean: 17.9 m), and 6.2–30.9 m (mean: 19.1 m), respectively (Figure 6). The midpoint of the euphotic layer, i.e.,  $Z_{10\%}(\text{PAR})$ , varied from 19.6 to 110.1 m, with an average depth of 56.4 m (Figure 6).

### 3.5. Contribution of CDOM and SPM Toward UV-B Attenuation

Overall, we found that  $a_{\text{CDOM}}$  at 305, 313, and 320 nm were approximately 1–2 orders of magnitude higher than their corresponding  $a_p(\lambda)$ . Specifically, the contribution of  $a_p(\lambda)$  toward nonwater absorption ( $a_{\text{nw}}(\lambda)$ ), ranged from 1.5 to 25.7%, 1.7 to 40.4%, and 1.4 to 30.2% at wavelengths 305, 313, and 320 nm, respectively (Figure 7), and was significantly different between those wavelengths ( $\chi^2 = 25.06$ ,  $df = 2$ ,  $p < 0.0001$ ). Pairwise comparison revealed that the contribution of  $a_p(\lambda)$  toward  $a_{\text{nw}}(\lambda)$  was significantly lower at 305 nm ( $7.1 \pm 0.2\%$ , mean  $\pm$  SEM)

**Table 3**

Summary of the Downwelling Diffuse Attenuation Coefficients ( $K_d$ , in  $m^{-1}$ ) for UV-B Wavelengths 305, 313, and 320 nm, the UV-A Wavelengths 340, 380, and 395 nm, as Well as the Integrated PAR (400–700 nm) Spectrum

Province	$K_d$ (305 nm)	$K_d$ (313 nm)	$K_d$ (320 nm)	$K_d$ (340 nm)	$K_d$ (380 nm)	$K_d$ (395 nm)	$K_d$ (PAR)
AUSE	0.230 $\pm$ 0.019	0.182 $\pm$ 0.015	0.164 $\pm$ 0.012	0.108 $\pm$ 0.005	0.073 $\pm$ 0.006	0.063 $\pm$ 0.004	0.060 $\pm$ 0.002
AUSW	0.191 $\pm$ 0.005	0.138 $\pm$ 0.012	0.128 $\pm$ 0.006	0.082 $\pm$ 0.006	0.049 $\pm$ 0.007	0.039 $\pm$ 0.007	0.038 $\pm$ 0.001
BENG*	0.313 $\pm$ NA	0.251 $\pm$ NA	0.228 $\pm$ NA	0.151 $\pm$ NA	0.095 $\pm$ NA	0.031 $\pm$ NA	0.069 $\pm$ NA
CARB	0.227 $\pm$ 0.028	0.165 $\pm$ 0.021	0.153 $\pm$ 0.017	0.100 $\pm$ 0.009	0.064 $\pm$ 0.009	0.052 $\pm$ 0.008	0.049 $\pm$ 0.006
EAFR	0.275 $\pm$ 0.086	0.226 $\pm$ 0.075	0.209 $\pm$ 0.074	0.147 $\pm$ 0.060	0.103 $\pm$ 0.054	0.093 $\pm$ 0.053	0.081 $\pm$ 0.036
ISSG	0.144 $\pm$ 0.008	0.110 $\pm$ 0.006	0.105 $\pm$ 0.005	0.074 $\pm$ 0.003	0.053 $\pm$ 0.002	0.044 $\pm$ 0.002	0.038 $\pm$ 0.001
NASE	0.168 $\pm$ 0.009	0.131 $\pm$ 0.007	0.119 $\pm$ 0.006	0.085 $\pm$ 0.005	0.053 $\pm$ 0.004	0.048 $\pm$ 0.005	0.043 $\pm$ 0.003
NATR	0.182 $\pm$ 0.009	0.139 $\pm$ 0.007	0.128 $\pm$ 0.005	0.082 $\pm$ 0.003	0.055 $\pm$ 0.004	0.050 $\pm$ 0.005	0.044 $\pm$ 0.003
NPTG	0.171 $\pm$ 0.011	0.128 $\pm$ 0.008	0.116 $\pm$ 0.007	0.074 $\pm$ 0.005	0.047 $\pm$ 0.004	0.039 $\pm$ 0.003	0.040 $\pm$ 0.002
PEQD	0.133 $\pm$ 0.010	0.119 $\pm$ 0.010	0.108 $\pm$ 0.006	0.073 $\pm$ 0.005	0.052 $\pm$ 0.004	0.046 $\pm$ 0.003	0.037 $\pm$ 0.008
PNEC	0.293 $\pm$ 0.034	0.226 $\pm$ 0.027	0.214 $\pm$ 0.026	0.150 $\pm$ 0.018	0.104 $\pm$ 0.011	0.093 $\pm$ 0.010	0.067 $\pm$ 0.003
SATL	0.156 $\pm$ 0.009	0.123 $\pm$ 0.008	0.115 $\pm$ 0.008	0.080 $\pm$ 0.005	0.044 $\pm$ 0.003	0.036 $\pm$ 0.002	0.036 $\pm$ 0.002
SPSG	0.108 $\pm$ 0.009	0.098 $\pm$ 0.004	0.100 $\pm$ 0.005	0.062 $\pm$ 0.004	0.046 $\pm$ 0.002	0.040 $\pm$ 0.002	0.036 $\pm$ 0.002
SSTC	0.245 $\pm$ 0.036	0.190 $\pm$ 0.029	0.172 $\pm$ 0.027	0.109 $\pm$ 0.022	0.070 $\pm$ 0.013	0.056 $\pm$ 0.013	0.046 $\pm$ 0.012
WTRA	0.215 $\pm$ 0.015	0.166 $\pm$ 0.012	0.148 $\pm$ 0.011	0.100 $\pm$ 0.007	0.068 $\pm$ 0.007	0.063 $\pm$ 0.008	0.058 $\pm$ 0.005
Overall	0.181 $\pm$ 0.006	0.142 $\pm$ 0.005	0.132 $\pm$ 0.005	0.089 $\pm$ 0.003	0.058 $\pm$ 0.002	0.050 $\pm$ 0.002	0.045 $\pm$ 0.001

Note. Data are shown by Longhurst's provinces that were visited as part of the Malaspina 2010 Expedition. Asterisk (\*) indicates province not included in the Kruskal-Wallis test. Values are mean  $\pm$  SEM.

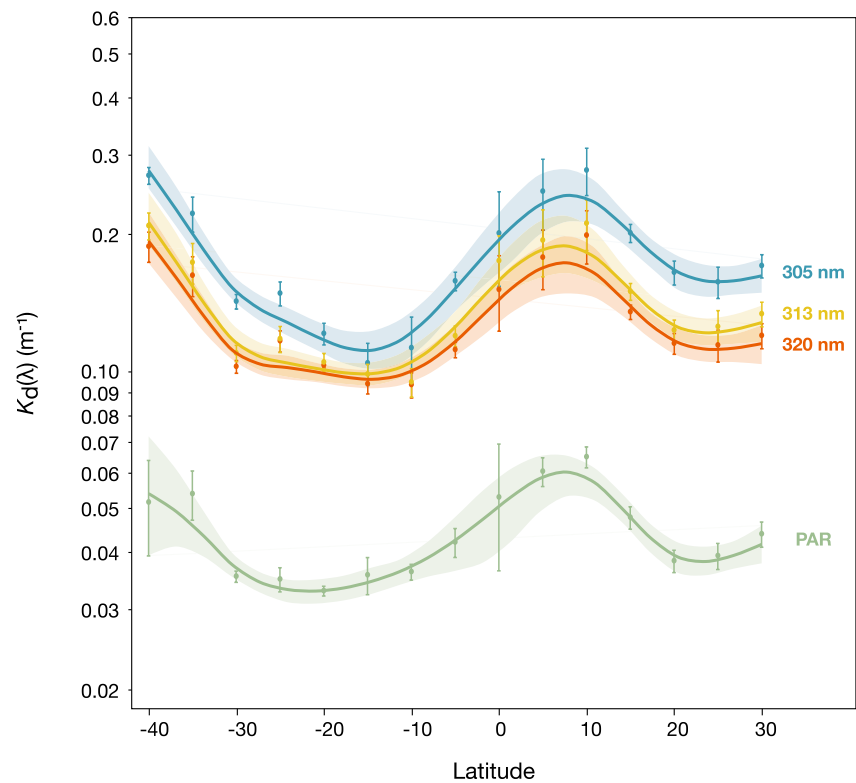


**Figure 5.** Mean  $\pm$  SEM  $K_d(\lambda)$  ( $\text{m}^{-1}$ ) of 305, 313, and 320 nm and photosynthetically active radiation (PAR) for 5-degree latitudinal bands in the subtropical and tropical ocean found during the Malaspina 2010 Expedition. Smoothing was performed at  $\lambda = 0.05$ . Shaded areas represent 95% confidence intervals.

than at 313 nm ( $8.3 \pm 0.2\%$ ,  $p < 0.0001$ ) and 320 nm ( $8.0 \pm 0.2\%$ ,  $p < 0.001$ ). No difference was found between 313 and 320 nm. Comparing the contribution of  $a_p(\lambda)$  between Longhurst's provinces revealed an overall significant difference at 305 ( $\chi^2 = 28.86$ ,  $df = 13$ ,  $p = 0.01$ ), 313 ( $\chi^2 = 26.81$ ,  $df = 13$ ,  $p < 0.05$ ), and 320 nm ( $\chi^2 = 29.99$ ,  $df = 13$ ,  $p < 0.01$ ). Pairwise comparison showed that the contribution of  $a_p(\lambda)$  toward  $a_{nw}(\lambda)$  was significantly lower in NASE than in ISSG at 305 ( $p < 0.01$ ) and 313 nm ( $p < 0.05$ ; Figure S2 in Supporting Information S1). At 305 nm, the contribution of  $a_p(\lambda)$  found in NASE was also significantly lower compared to NPTG ( $p < 0.05$ ).

Chl-*a* concentration,  $a_{CDOM}(\lambda)$ , and  $a_p(\lambda)$  all significantly correlated with  $K_d(\lambda)$  at wavelengths 305, 313, and 320 nm (Figure 8, Table S1 in Supporting Information S1). The strongest correlation was found between  $K_d(\lambda)$  and Chl-*a* concentration, with  $r$  ranging from 0.71 to 0.76 at UV-B wavelengths ( $p < 0.001$ ), and  $r = 0.82$  for PAR ( $p < 0.001$ ). The correlation coefficient between  $K_d(\lambda)$  and  $a_{CDOM}(\lambda)$  was relatively constant across UV-B wavelengths ( $r = 0.48$ – $0.50$ ,  $p < 0.001$ ), but increased for  $K_d(\lambda)$  and  $a_p(\lambda)$  with increasing wavelength ( $r = 0.38$ – $0.49$ ,  $p < 0.001$ ). At each UV-B wavelength, temperature correlated with  $a_{CDOM}(\lambda)$ ;  $r = 0.18$ – $0.22$ ,  $p < 0.05$ ) but more strongly with  $a_p(\lambda)$ ;  $r = 0.24$ – $0.29$ ,  $p < 0.01$ ).

We found that the multiple linear regression analysis to predict  $K_d(\lambda)$  was significantly improved when Chl-*a* was included as an independent variable, as the residual error was large when Chl-*a* was not included ( $R^2$ : 0.26–0.33). In comparison, the multiple linear regression analysis to predict  $K_d(\lambda)$  based on Chl-*a*,  $a_{CDOM}(\lambda)$ , and  $a_p(\lambda)$  identified significant regression equations at UV-B wavelengths 305, 313, and 320 nm (overall models:  $p < 0.0001$ ; Table 4). However, whereas Chl-*a* concentration (which is correlated to absorption and backscattering) and  $a_{CDOM}(\lambda)$  were both significant explanatory variables ( $p < 0.01$ ) at each UV-B wavelength,  $a_p(\lambda)$  was not a significant explanatory variable and therefore removed from the model. At all three wavelengths, the  $R^2$  values of the multilinear regression (305 nm: 0.57; 313 nm: 0.59; 320 nm: 0.59) were considerably higher compared to the  $R^2$  of linear regressions to predict  $K_d$  based on Chl-*a* concentration alone (305 nm: 0.51; 313 nm: 0.54; 320 nm: 0.53), which suggests that the incorporation of  $a_{CDOM}(\lambda)$  into the model improves the prediction of  $K_d$  in the UV-B spectrum.

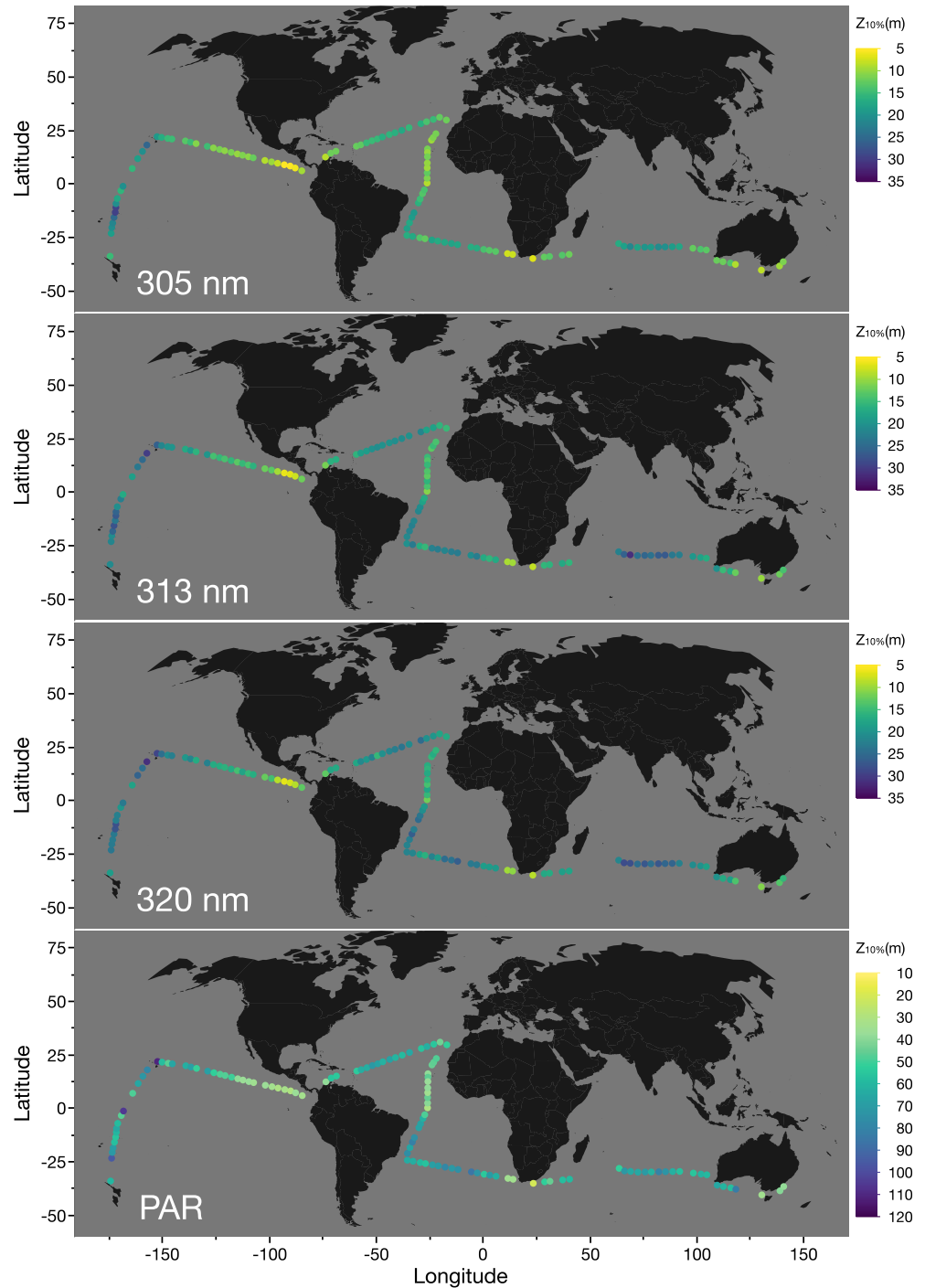


**Figure 6.** Ten percent attenuation depths ( $Z_{10\%}$ , in m) of the UV-B wavelengths 305 nm, 313 nm, 320 nm, and of the integrated photosynthetically active radiation (PAR) spectrum (400–700 nm) measured during the Malaspina 2010 Expedition.

#### 4. Discussion

The relative contributions of CDOM and SPM toward UVR absorption differed considerably between wavelengths but only little between provinces. We determined  $K_d(\lambda)$  values as low as 0.079, 0.074, and 0.074  $\text{m}^{-1}$  for 305, 313, and 320 nm, respectively (Table 2), and a minimum  $K_d(\text{PAR})$  of 0.021  $\text{m}^{-1}$ , identifying these waters, located in the Longhurst's provinces ISSG and SPSG, as the clearest oceanic waters thus far reported.

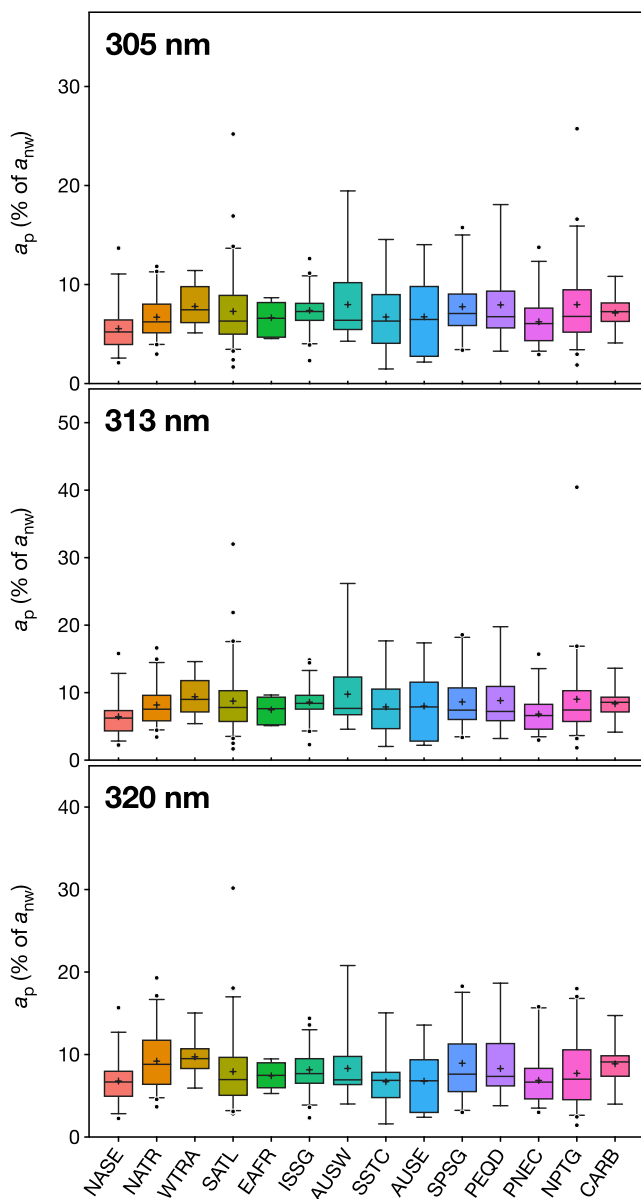


**Figure 7.** Contribution of  $a_p$  (in %) toward total nonwater absorption ( $a_{nw}$ ) at the wavelengths 305, 313, and 320 nm for each of the 14 Longhurst's provinces visited as part of the Malaspina 2010 Expedition. The horizontal line in plots shows the median, crosses represent the mean, while whiskers indicate the upper and lower 95% confidence intervals.

Tedetti et al. (2007) reported that UVR and PAR could penetrate to extreme depths in the water column of the South Pacific Gyre ( $Z_{10\%}(305 \text{ nm}) = 28 \text{ m}$ ;  $Z_{10\%}(340 \text{ nm}) = 59 \text{ m}$ ), and determined  $K_d(\lambda)$  values as low as 0.083, 0.039, and  $0.027 \text{ m}^{-1}$  for 305 and 340 nm and PAR, respectively. The same authors concluded that certain regions of the South Pacific Gyre are more optically transparent than the previously reported clearest oceanic waters, e.g., the subtropical Atlantic Ocean (Obernosterer et al., 2001). Another study in the South Pacific Gyre reported a similarly low attenuation of UVR and PAR, with a minimum  $K_d(310 \text{ nm})$  of  $0.068 \text{ m}^{-1}$ , and a mean  $K_d(\text{PAR})$  for the four clearest stations of  $0.0352 \text{ m}^{-1}$  (Morel, Gentili et al., 2007). Previous reports agree that the central hyper-oligotrophic region of the South Pacific gyre contains the “clearest” oceanic waters, whereas we found that the location where minimal attenuation could be observed varied between wavelengths. For example, 305-nm wavelengths penetrated furthest into the water column in province SPSG at the western boundary of the South Pacific Gyre. In the case of 313 nm, minimal attenuation was measured in the center of the Indian Ocean (ISSG), which was previously grossly undersampled, while for the remaining four UVR wavelengths (320, 340, 380, 395 nm) and PAR,  $K_d(\lambda)$  was lowest in the North Pacific Tropical Gyre (NPTG) around the Hawaiian Islands. This finding highlights that the concept of the world's clearest marine waters is wavelength-dependent. Moreover, although we only sampled each station one time along the global expedition, optical properties are expected to be dynamic, a consequence of continuous and seasonally driven oceanographic processes that regulate the stocks of constituents absorbing solar radiation, including phytoplankton blooms, cell lysis processes releasing dissolved organic carbon, and the microbial transformation and cycling of CDOM and SPM. Since both components have distinct optical properties and peak-absorption wavelengths, we could observe a considerable variation in their UVR absorption coefficients.

The lowest  $a_{\text{CDOM}}(\lambda)$  at UV-B wavelengths was found at station 61 in the Indian Ocean province ISSG (305 nm:  $0.096 \text{ m}^{-1}$ , 313 nm:  $0.072 \text{ m}^{-1}$ , 320 nm:  $0.065 \text{ m}^{-1}$ ). ISSG also exhibited the lowest average  $a_{\text{CDOM}}(\lambda)$  of all provinces (305 nm:  $0.139 \text{ m}^{-1}$ , 313 nm:  $0.109 \text{ m}^{-1}$ , 320 nm:  $0.101 \text{ m}^{-1}$ ), as already noticed by Iuculano et al. (2019), who investigated  $a_{\text{CDOM}}$  at 254 and 325 nm. Since remote regions of the ocean generally receive negligible terrestrial CDOM inputs, the majority of CDOM originates from phytoplankton-related processes and microbial transformation of the materials released (Nelson et al., 2010). The lowest  $a_{\text{CDOM}}(\lambda)$  values found in ISSG are consistent with the very low phytoplanktonic stocks in these Indian Ocean waters between the sea surface and 20% PAR depth (Chl-*a*:  $0.079 \pm 0.006 \text{ mg m}^{-3}$ , mean  $\pm$  SEM; Table 1). Correspondingly, two studies recently reported exceptionally low phytoplankton biomass in this region, based on Chl-*a* measurements and picophytoplankton cell counts (Agusti et al., 2019; Iuculano et al., 2019). In contrast, the strongest UV-B absorption by CDOM was detected at the two stations corresponding to upwelling-affected areas.

One station was in the PNEC province near the Costa Rica Thermal Dome (CRTD) upwelling system (Cromwell, 1958), which causes a continuous replenishment of nutrients that fuel phytoplankton growth and biological production (Fiedler, 2002; Kessler, 2006). Another upwelling site is off the South African coast (station 43 in province SATL), where nutrient-rich cold waters are being upwelled to form the highly productive Benguela current (Garzoli & Gordon, 1996; Hutchings et al., 2009; Lamont et al., 2014). The high productivity in upwelling regions leads to elevated  $a_{\text{CDOM}}(\lambda)$  and reduced UV-B penetration. Several studies have reported a hemispherical asymmetry in  $\text{Si}(\text{OH})_4$  and  $\text{NO}_3$  concentrations at equatorial upwelling sites, with higher concentrations north of the equator (Dugdale et al., 2002; Jiang & Chai, 2005; Levitus et al., 1993). Due to this asymmetry, chlorophyll concentrations and phytoplankton carbon biomass are higher north of the equator (Estrada et al., 2016; Wang

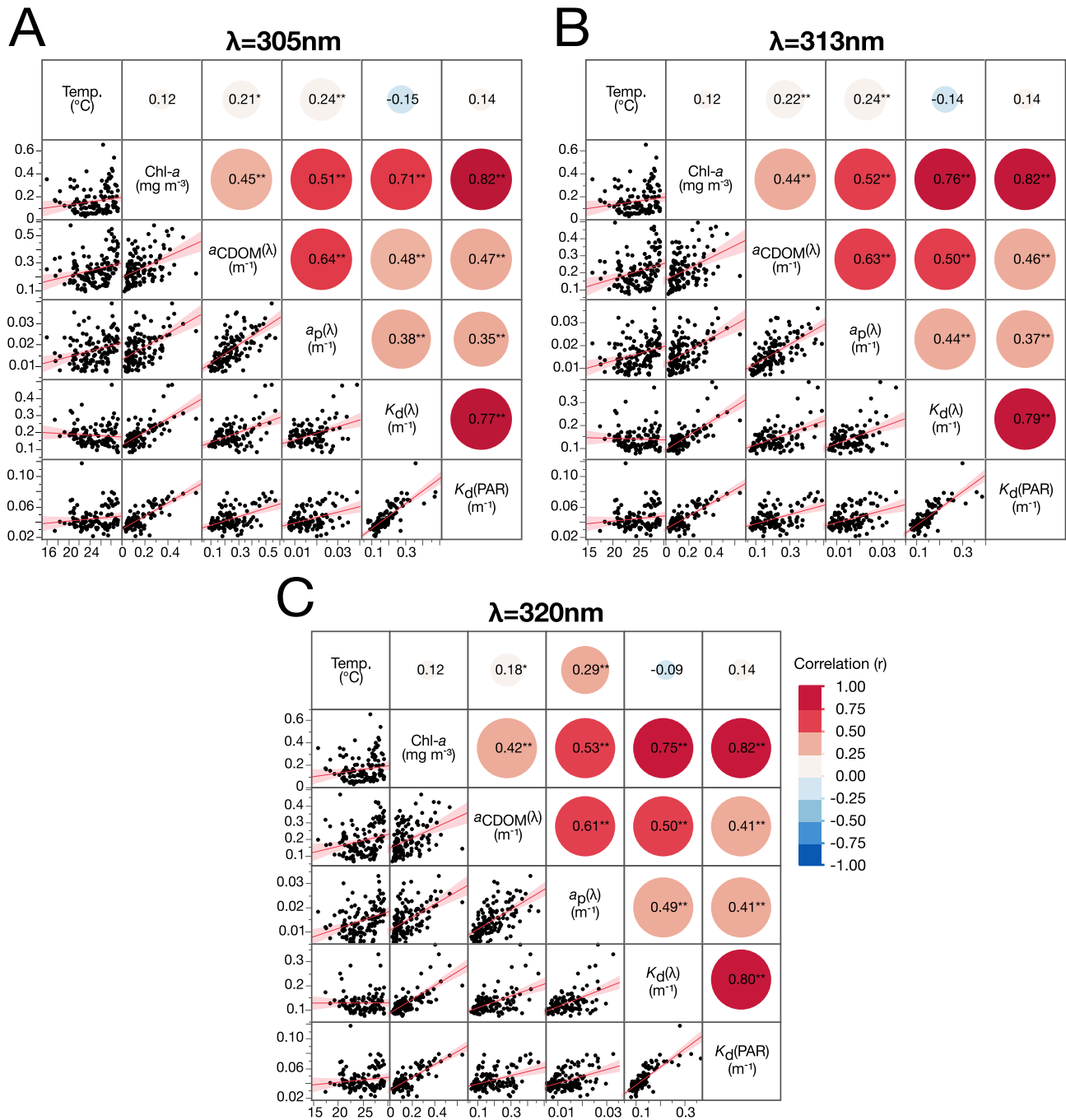


**Figure 8.** Results of the correlation analysis between sea surface temperature,  $K_d(\text{PAR})$ , depth-weighted (surface to 20% PAR depth) Chl-*a* concentration,  $a_{\text{CDOM}}(\lambda)$  and  $a_p(\lambda)$ , and  $K_d(\lambda)$  at the UV-B wavelengths ( $\lambda$ ) 305 nm (a), 313 nm (b), and 320 nm (c). The red lines and shaded areas represent the correlation line and 95% CIs, respectively. The colors of the circles and the values therein indicate the magnitude of the Pearson correlation coefficient ( $r$ ). The sizes of circles denote the probability value ( $p$ ) of the pairwise correlation analysis while asterisks highlight instances where  $p < 0.05$  (\*) or  $p < 0.001$  (\*\*).

et al., 2013), which could explain why  $K_d(305)$  and  $K_d(313)$  were on average higher at 5°–10°N than in the 5°–15°S latitudinal band.

Despite the 1–2 orders lower magnitude of UV-B absorption by particles compared to CDOM, the pattern observed for  $a_p(\lambda)$  generally mirrored that of  $a_{\text{CDOM}}(\lambda)$ , with the lowest and highest average values measured in provinces ISSG and PNEC, respectively (Table 1). However, while  $a_{\text{CDOM}}(\lambda)$  reached maxima closest to the Costa Rica Dome in PNEC, the highest  $a_p(\lambda)$  was detected further offshore in PNEC (station 124), approximately

**Table 4**

Results of the Multiple Linear Regression Analysis to Predict the Downwelling Diffuse Attenuation Coefficient ( $K_d$ ) at 305, 313, and 320 nm, Based on the Respective Depth-Weighted (Surface to 20% PAR Depth) Absorption Coefficients of CDOM ( $a_{CDOM}$ ) and Total Particulate Matter ( $a_p$ ), and Chlorophyll-*a* Concentration (Chl-*a*, in  $mg\ m^{-3}$ )

Dependent variable	Explanatory variables/model	<i>t</i>	$\beta$ coefficient	95% CI ( $\pm$ )	<i>p</i> -value	<i>F</i>	<i>R</i> <sup>2</sup>
$K_d$ (305 nm)	$a_{CDOM}$ (305 nm)	3.60	0.3098	0.105	0.0005*	12.990	0.25
	$a_p$ (305 nm)	n.s.	n.s.	n.s.	0.1845	n.s.	0.17
	Chl- <i>a</i>	8.54	0.6469	0.084	<0.0001*	72.970	0.51
	Overall model	–	–	–	<0.0001*	46.829	0.57
$K_d$ (313 nm)	$a_{CDOM}$ (313 nm)	3.26	0.2689	0.085	0.0014*	10.658	0.25
	$a_p$ (313 nm)	n.s.	n.s.	n.s.	0.4711	n.s.	0.20
	Chl- <i>a</i>	8.85	0.6557	0.063	<0.0001*	78.349	0.54
	Overall model	–	–	–	<0.0001*	51.230	0.59
$K_d$ (320 nm)	$a_{CDOM}$ (320 nm)	2.91	0.2361	0.081	0.0045*	8.474	0.24
	$a_p$ (320 nm)	n.s.	n.s.	n.s.	0.7317	n.s.	0.25
	Chl- <i>a</i>	8.37	0.6207	0.058	<0.0001*	70.019	0.53
	Overall model	–	–	–	<0.0001*	50.122	0.59

Note. n.s. denotes “not significant.” \* $p < 0.05$ .

650 km north-west of the dome. “The large inputs of Saharan dust ( $\sim 180\ Tg\ yr^{-1}$ ; Jickells et al., 2005) to Eastern Atlantic waters (NATR and WTRA; Pabortsava et al., 2017) could potentially explain why  $a_p(\lambda)$  and  $K_d(UV)$  were relatively high here but  $a_{CDOM}(\lambda)$  was not (Figures S3 and S4 in Supporting Information S1). Aeolian dust fluxes from arid regions represent iron sources for nutrient-poor regions of the ocean (Gao et al., 2001; Mahowald et al., 2005) that can stimulate the growth and activity of bacterioplankton (Marañon et al., 2010) and phytoplankton (Baker et al., 2007; Moore et al., 2006). Iron concentrations are unusually high in the Eastern Tropical Atlantic (Bowie et al., 2002; Pinedo-González et al., 2015) and the water column between the surface to 20% PAR depth is characterized by high chlorophyll concentrations ( $>0.6\ mg\ m^{-3}$ ). Here, the phytoplankton community was dominated by coccolithophores ( $\sim 30,000\ cells\ L^{-1}$ ; Estrada et al., 2016), which can backscatter a large proportion of incoming UVR (Quintero-Torres et al., 2006), unlike cyanobacteria (Morel et al., 1993; Vaillancourt et al., 2004).

Additionally, suspended mineral dust particles could also directly (i.e., not mediated by phytoplankton) significantly contribute to the backscattering of UVR. Indeed, several studies have reported that the mass-specific absorption and backscattering coefficients of mineral dust in general (Bowers & Binding, 2006), and of Saharan dust in particular (Stramski et al., 2007), increases exponentially from the far end of the PAR spectrum toward short UV-B wavelengths. This finding supports the idea that UV-B backscattering by mineral particles could be considerable at locations characterized by atmospheric dust deposition, as previously suggested for light in the ocean (Stramski et al., 2004). Further evidence of the strong influence of (non)algal particles on the optical properties in this region includes the high  $K_d$  values measured here for UV-A wavelengths and PAR, which are both not strongly absorbed by CDOM.

Our results provide an assessment of the contribution of suspended particulate matter in the upper ocean to UV-B absorption across the global oligotrophic ocean. Several studies have derived the absorption and scattering coefficients of particulate matter in natural marine waters from in situ measurements or ocean color remote sensing, thereby generating extensive reference data sets (Boss et al., 2013; Bricaud et al., 1998). However, existing studies have primarily focused on PAR and largely disregarded UVR, and UV-B wavelengths in particular. Past studies reported particulate absorption studies to date down to the blue range of the spectra (wavelength 400 nm), reporting mean  $a_p(400\ nm)$  of  $\sim 0.001$ , 0.032, and  $0.142\ m^{-1}$  in waters with Chl-*a* concentrations of  $<0.1$ , 0.1–1.0, and  $>1\ mg\ m^{-3}$ , respectively (Boss et al., 2013). We determined an overall mean  $a_p(400\ nm)$  of  $0.011\ m^{-1}$  (range 0.003–0.039  $m^{-1}$ , Figure 3) across the oligotrophic ocean.

In the Sargasso Sea, Morrow et al. (1989) measured  $a_p(400\ nm)$  of  $\sim 0.014\ m^{-1}$  in surface waters (20-m depth) in March, while other studies reported  $a_p(400\ nm)$  of  $0.021\ m^{-1}$  in April (Garver et al., 1994) and 0.003–0.004  $m^{-1}$

in September/October (Bricaud & Stramski, 1990). In the present study, we found a water column-averaged  $a_p(400\text{ nm})$  of  $0.009\text{ m}^{-1}$  (range:  $0.004\text{--}0.022\text{ m}^{-1}$ ) at the five NATR stations in the Sargasso Sea (st. 134–138) in June/July (Figure 3), toward the lower end of previously reported values. For surface waters (0–30 m) of the oligotrophic North-Pacific and South-Pacific, Garver et al. (1994) reported  $a_p(400\text{ nm})$  of 0.021 (NPTG) and  $0.018\text{ m}^{-1}$  (SPSG), respectively. In the present study, we determined a slightly lower mean ( $\pm$ SEM)  $a_p(400\text{ nm})$  of  $0.013 \pm 0.001$  and  $0.015 \pm 0.001\text{ m}^{-1}$  for NPTG and SPSG, respectively. These previous reports of  $a_p(400\text{ nm})$  in the Pacific Ocean were based on measurements done in December-February, which are similar to the  $a_p(400\text{ nm})$  values we obtained in April-May.

Downwelling attenuation coefficients ( $K_d$ ) were most strongly correlated with Chl-*a*, followed by either surface water  $a_{\text{CDOM}}(\lambda)$  or  $a_p(\lambda)$  depending on the wavelength (Figure 8). Multiple studies have reported significant linear correlations between Chl-*a* and  $K_d(\text{UV})$  in coastal and open ocean waters (Figuerola, 2002; Morel, Claustre et al., 2007; Stambler et al., 1997), which were mostly explained by the covariance of Chl-*a* and CDOM as the primary UVR absorber (Bricaud et al., 1981; Coble et al., 2004). Yet, we identified that despite CDOM being the principal UVR absorber, the correlation between ( $K_d$ ) and  $a_{\text{CDOM}}(\lambda)$  at UVR wavelengths was only moderately strong (Figure 8) and  $a_{\text{CDOM}}(\lambda)$  was not a main explanatory variable for UVR attenuation (Table 4), representing an apparent paradox. While  $a_p(\lambda)$  and  $a_{\text{CDOM}}(\lambda)$  at UV-B wavelengths were both lowest in the Indian Ocean province ISSG (see also Iuculano et al., 2019),  $K_d$  was minimal in the South Pacific province SPSG. Those findings highlight the complex relationship between apparent (e.g.,  $K_d$ ) and inherent ( $a_{\text{CDOM}}(\lambda)$  and  $a_p(\lambda)$ ) optical properties and indicate that other processes besides UVR absorption play an important role in determining the underwater UV environment (Reynolds et al., 2001; Vaillancourt et al., 2004). For example, it could be that the extend of backscattering by algal and mineral particles (determined by the particles' composition, geometry and size) varied in the water column between the two provinces. However, information about backscattering of UV wavelengths compared to PAR is still limited to date (Stramski et al., 2004).

Even though the mean ( $\pm$ SEM)  $K_d(\text{UV-B})$  determined for ISSG stations ( $K_d(305\text{ nm}) = 0.144 \pm 0.008\text{ m}^{-1}$ ,  $K_d(313\text{ nm}) = 0.110 \pm 0.006\text{ m}^{-1}$ ,  $K_d(320\text{ nm}) = 0.105 \pm 0.005\text{ m}^{-1}$ ) were not as low as those obtained at SPSG (Table 3), they were still remarkably low in the global context. Furthermore, we identified a section within ISSG, spanning a total distance of  $\sim 2,900\text{ km}$  (stations 54–63), where the water column was exceptionally transparent to UV-B. Here, we measured mean ( $\pm$ SEM)  $K_d$  of  $0.123 \pm 0.003$ ,  $0.093 \pm 0.003$ , and  $0.092 \pm 0.003\text{ m}^{-1}$  for the wavelengths 305, 313, and 320 nm, respectively, which identifies this central sector of the ISSG among the most UV-B-transparent worldwide (Morel, Gentili et al., 2007; Tedetti & Sempere, 2006). In fact, we determined biologically effective optical depths (i.e.,  $Z_{10\%}$ ) of  $18.7 \pm 0.5$ ,  $25.0 \pm 0.9$ , and  $25.2 \pm 0.7\text{ m}$  (mean  $\pm$  SEM) for the wavelengths 305, 313, and 320 nm, respectively, in the central region of ISSG. These  $Z_{10\%}$  depths are deeper than those of most other oligotrophic marine waters, including the Red Sea ( $Z_{10\%}(305\text{ nm})$ : 13.7 m; Overmans & Agusti, 2019), the western Mediterranean Sea ( $Z_{10\%}(305\text{ nm})$ : 10–11 m; Llabres et al., 2010; Sempere et al., 2015), the central subtropical Atlantic Ocean ( $Z_{10\%}(305\text{ nm})$ : 16 m), or the Gulf of Mexico ( $Z_{10\%}(305\text{ nm})$ : 13 m; Obernosterer et al., 2001; Tedetti & Sempere, 2006; Weinbauer et al., 1997), and only comparable to those reported in the South Pacific Gyre ( $Z_{10\%}(305\text{ nm})$ : 27.7 m; Tedetti et al., 2007). In comparison, we found a mean ( $\pm$ SEM)  $Z_{10\%}(305\text{ nm})$  of  $22.3 \pm 1.8\text{ m}$  for the South Pacific province SPSG but identified two SPSG stations (st. 87 and 88) where  $Z_{10\%}(305\text{ nm})$  was 29.2 m (Figure 6), and therefore deeper than in the South Pacific Gyre (Tedetti et al., 2007). These findings highlight that, across the global oligotrophic ocean, marine organisms are likely exposed to potentially harmful UV-B levels down to depths of  $\sim 25\text{--}30\text{ m}$ . A study by Catala et al. (2016), who sampled the same locations, found that the mixed layer depth (MLD) ranged from 8-m to 100-m depth, averaging  $48 \pm 21\text{ m}$  (mean  $\pm$  SD). This finding shows that the majority of sampled locations are characterized by an MLD that is well below the  $Z_{10\%}(305\text{ nm})$  depth calculated here.

We could observe that open ocean waters between the equator and  $15^\circ\text{S}$  were considerably more transparent to UV-B than the waters between the equator and  $15^\circ\text{N}$ . This difference in optical properties between northern and southern tropical waters is of particular relevance since several other ecologically relevant differences between the two hemispheres have been identified. For example, based on cloud fraction data from the year 2010 (data obtained from [https://earthobservatory.nasa.gov/global-maps/MODAL2\\_M\\_CLD\\_FR](https://earthobservatory.nasa.gov/global-maps/MODAL2_M_CLD_FR)), we found that in late spring, summer, and autumn the region between the equator and  $15.5^\circ\text{S}$  experienced significantly less cloud cover than the region between the equator and  $15.5^\circ\text{N}$  (see Figure S8 in Supporting Information S1). This finding suggests that cloud-driven UV attenuation in the atmosphere is lower in the southern tropics than in the northern



tropics. While the degree of atmospheric UV attenuation does not affect the transparency of the water column, it is of biological relevance since it determines how much UV is received at the water surface.

Additionally, several studies have reported an asymmetry in stratospheric ozone and incident UV-B between the northern and southern hemispheres (Barnes et al., 2019; Weatherhead & Andersen, 2006). Specifically, stratospheric ozone levels in spring and summer decreased between 1970 and 2012 by 11.0% in the southern and 2.7% in the northern hemispheres, indicating higher incident UV-B at sea level in southern latitudes (Agusti et al., 2015). The previous findings of considerably higher UV-B irradiances in the southern hemisphere, and our result that marine waters between the equator and 15°S were highly transparent, suggest that UV-B represents a significant stressor for marine organisms in this region. Studies by Agusti et al. (2015) and Llabres et al. (2013) found that overall, marine biota from the southern hemisphere were more resistant to UV-B than their northern hemisphere counterparts. Certain organisms such as echinoderms or organisms in early life stages exhibited significant differences in UV-B sensitivity between northern and southern individuals (Agusti et al., 2015). This finding suggests a strong evolutionary selection of UV-B resistant organisms and genotypes in the southern hemisphere as results of the high UV-B exposure (Paul & Gwynn-Jones, 2003).

Our study clearly showed that CDOM was the primary UV-B absorber, while the contribution of particulate absorption toward total nonwater absorption ( $a_{nw}(\lambda)$ ) varied significantly between wavelengths as well as Longhurst's provinces. The relative contribution of  $a_p(\lambda)$  toward  $a_{nw}(\lambda)$  was significantly lower at 305 nm ( $7.1 \pm 0.2\%$ , mean  $\pm$  SEM) than at 313 nm ( $8.3 \pm 0.2\%$ ) and 320 nm ( $8.0 \pm 0.2\%$ ), due to the more pronounced exponential increase of  $a_{CDOM}(\lambda)$  compared to  $a_p(\lambda)$  with decreasing wavelength (Babin et al., 2003; Bricaud et al., 1981). In comparison, Nelson and Siegel (2013) reported that the average contributions of  $a_p(\lambda)$  toward  $a_{nw}(\lambda)$  across various ocean basins were 14.0%, 18.3%, and 21.7% at 305, 313, and 320 nm, respectively. The lower relative contribution found in our study reflects the fact that we almost exclusively sampled oligotrophic waters, compared to the more productive coastal stations Nelson and Siegel (2013) included. In fact, a study based in the South-East Pacific found that east of the South Pacific gyre, where Chl-*a* concentrations were  $0.11 \text{ mg m}^{-3}$ , the contributions of  $a_p(\lambda)$  toward  $a_{nw}(\lambda)$  at 305, 313, and 320 nm were 39.7%, 30.2%, and 32.4%, respectively (Morel, Claustre et al., 2007). At the eastern boundary of the gyre (Chl-*a*:  $0.045 \text{ mg m}^{-3}$ ), the contributions of  $a_p(\lambda)$  toward  $a_{nw}(\lambda)$  at 305, 313, and 320 nm were 32.4%, 28.1%, and 29.5%, respectively, while inside the highly oligotrophic (Chl-*a*:  $0.032 \text{ mg m}^{-3}$ ) gyre,  $a_p(\lambda)$  represented 20.6% and 22.0% of  $a_{nw}(\lambda)$  at 313 and 320 nm, respectively (no data provided for 305 nm; Morel, Gentili et al., 2007). Those results indicate that the contribution of  $a_p(\lambda)$  toward  $a_{nw}(\lambda)$  decreases with decreasing Chl-*a* in the UV-B waveband, which is in agreement with other reports suggesting that phytoplankton has a negligible impact on absorption in highly oligotrophic areas (Nelson et al., 1998). We found strong correlations between  $a_{CDOM}(\lambda)$ ,  $a_p(\lambda)$ , and Chl-*a* across UV-B wavelengths. The robust correlation between Chl-*a* and  $a_p(\lambda)$  suggests that particulate absorption of UV-B wavelengths was predominantly due to phytoplankton.

## 5. Conclusion

The present study provides an assessment of UVR penetration and the contributing properties across the oligotrophic ocean, identifying CDOM as the main driver of UVR penetration in the oligotrophic ocean, followed by absorption by particles, largely dominated by phytoplankton and bacteria. However, only contributions to the absorption component of UVR attenuation were investigated as part of this study while the contribution of scattering in this spectrum was not determined and still remains not well understood. Biologically harmful UV-B exposures, as described by  $Z_{10\%}(320)$ , are received down to about 20-m depth across the oligotrophic ocean, which helps to explain the relatively low phytoplankton abundance in the top layer of the photic zone, characteristic of the open ocean (Agusti et al., 2019). We identified the most transparent waters between 5°S and 15°S in the subtropical Indian Ocean and the South Pacific, although the present expedition did not sample the hyper-oligotrophic region of the South Pacific gyre, which is known to contain the most transparent waters in the global ocean.

## Conflict of Interest

The authors declare no conflicts of interest relevant to this study.

## Data Availability Statement

The data set generated as part of this study can be accessed in the data repository Mendeley Data ([MALASPINA 2010 optical data: aCDOM\\_aParticles\\_Kd\\_Z10%](#)).

## Acknowledgments

This study was funded by the Spanish Ministry of Economy and Competitiveness through the Malaspina 2010 Expedition project (Consolider-Ingenio 2010; MICINN CSD2008-00077). The PhD fellowship of SO was supported by the baseline funding from KAUST to S. Agustí under award number BAS/1/1072-01-01. We would like to express special thanks Daffne López-Sandoval for processing the cloud fraction data, and to the captain and crew of the R/V Hespérides for their expert support and assistance during the expedition.

## References

- Agusti, S., Llabres, M., Carreja, B., Fernandez, M., & Duarte, C. M. (2015). Contrasting sensitivity of marine biota to UV-B radiation between southern and northern hemispheres. *Estuaries and Coasts*, *38*(4), 1126–1133. <https://doi.org/10.1007/s12237-014-9790-9>
- Agusti, S., Lubián, L. M., Moreno-Ostos, E., Estrada, M., & Duarte, C. M. (2019). Projected changes in photosynthetic picoplankton in a warmer subtropical ocean. *Frontiers in Marine Science*, *5*, 506. <https://doi.org/10.3389/fmars.2018.00506>
- Andrew, A. A., Del Vecchio, R., Subramaniam, A., & Blough, N. V. (2013). Chromophoric dissolved organic matter (CDOM) in the Equatorial Atlantic Ocean: Optical properties and their relation to CDOM structure and source. *Marine Chemistry*, *148*, 33–43. <https://doi.org/10.1016/j.marchem.2012.11.001>
- Babin, M., Stramski, D., Ferrari, G. M., Claustre, H., Bricaud, A., Obolensky, G., & Hoepffner, N. (2003). Variations in the light absorption coefficients of phytoplankton, nonalgal particles, and dissolved organic matter in coastal waters around Europe. *Journal of Geophysical Research*, *108*(C7), 3211. <https://doi.org/10.1029/2001JC000882>
- Baker, A. R., Weston, K., Kelly, S. D., Voss, M., Streu, P., & Cape, J. N. (2007). Dry and wet deposition of nutrients from the tropical Atlantic atmosphere: Links to primary productivity and nitrogen fixation. *Deep Sea Research Part I*, *54*(10), 1704–1720. <https://doi.org/10.1016/j.dsr.2007.07.001>
- Ban, S., Ohi, N., Leong, S. C. Y., Takahashi, K. T., Riser, C. W., & Taguchi, S. (2007). Effect of solar ultraviolet radiation on survival of krill larvae and copepods in Antarctic Ocean. *Polar Biology*, *30*(10), 1295–1302. <https://doi.org/10.1007/s00300-007-0290-2>
- Barnes, P. W., Williamson, C. E., Lucas, R. M., Robinson, S. A., Madronich, S., Paul, N. D., et al. (2019). Ozone depletion, ultraviolet radiation, climate change and prospects for a sustainable future. *Nature Sustainability*, *2*, 569–579. <https://doi.org/10.1038/s41893-019-0314-2>
- Berto, S., De Laurentiis, E., Tota, T., Chiavazza, E., Daniele, P. G., Minella, M., et al. (2016). Properties of the humic-like material arising from the photo-transformation of L-tyrosine. *Science of the Total Environment*, *546*, 434–444. <https://doi.org/10.1016/j.scitotenv.2015.12.047>
- Boss, E., Picheral, M., Leeuw, T., Chase, A., Karsenti, E., Gorsky, G., et al. (2013). The characteristics of particulate absorption, scattering and attenuation coefficients in the surface ocean: Contribution of the Tara Oceans Expedition. *Methods in Oceanography*, *7*, 52–62. <https://doi.org/10.1016/j.mio.2013.11.002>
- Bowers, D. G., & Binding, C. E. (2006). The optical properties of mineral suspended particles: A review and synthesis. *Estuarine, Coastal and Shelf Science*, *67*(1–2), 219–230. <https://doi.org/10.1016/j.ecss.2005.11.010>
- Bowie, A. R., Whitworth, D. J., Achterberg, E. P., Mantoura, R. F. C., & Worsfold, P. J. (2002). Biogeochemistry of Fe and other trace elements (Al, Co, Ni) in the upper Atlantic Ocean. *Deep Sea Research Part I*, *49*(4), 605–636. [https://doi.org/10.1016/S0967-0637\(01\)00061-9](https://doi.org/10.1016/S0967-0637(01)00061-9)
- Bricaud, A., Babin, M., Claustre, H., Ras, J., & Tiede, F. (2010). Light absorption properties and absorption budget of Southeast Pacific waters. *Journal of Geophysical Research*, *115*, C08009. <https://doi.org/10.1029/2009JC005517>
- Bricaud, A., Morel, A., Babin, M., Allali, K., & Claustre, H. (1998). Variations of light absorption by suspended particles with chlorophyll a concentration in oceanic (case 1) waters: Analysis and implications for bio-optical models. *Journal of Geophysical Research*, *103*(C13), 31033–31044. <https://doi.org/10.1029/98JC02712>
- Bricaud, A., Morel, A., & Prieur, L. (1981). Absorption by dissolved organic-matter of the sea (yellow substance) in the UV and visible domains. *Limnology & Oceanography*, *26*(1), 43–53. <https://doi.org/10.4319/lo.1981.26.1.0043>
- Bricaud, A., & Stramski, D. (1990). Spectral absorption-coefficients of living phytoplankton and nonalgal biogenous matter—A comparison between the Peru upwelling area and the Sargasso Sea. *Limnology & Oceanography*, *35*(3), 562–582. <https://doi.org/10.4319/lo.1990.35.3.0562>
- Catala, T. S., Alvarez-Salgado, X. A., Otero, J., Iuculano, F., Companys, B., Horstkotte, B., et al. (2016). Drivers of fluorescent dissolved organic matter in the global epipelagic ocean. *Limnology & Oceanography*, *61*(3), 1101–1119. <https://doi.org/10.1002/lno.10281>
- Coble, P. G., Zepp, R. G., & Zika, R. G. (2004). CDOM in the ocean: Transformation processes and their effects on optical properties. *Marine Chemistry*, *89*(1–4), 1. <https://doi.org/10.1016/j.marchem.2004.06.001>
- Cromwell, T. (1958). Thermocline topography, horizontal currents and “ridging” in the eastern tropical Pacific. *Inter-American Tropical Tuna Commission Bulletin*, *3*(3), 133–164.
- Dishon, G., Dubinsky, Z., Fine, M., & Iluz, D. (2012). Underwater light field patterns in subtropical coastal waters: A case study from the Gulf of Eilat (Aqaba). *Israel Journal of Plant Sciences*, *60*(1–2), 265–275. <https://doi.org/10.1560/ijps.60.1-2.265>
- Downs, N. J., Schouten, P. W., & Parisi, A. V. (2013). Seasonal variations in the subsurface ultraviolet-B on an inshore Pacific coral reef ecosystem. *Photochemistry and Photobiology*, *89*(5), 1234–1243. <https://doi.org/10.1111/php.12101>
- Duarte, C. M. (2015). Seafaring in the 21st century: The Malaspina 2010 Circumnavigation Expedition. *Limnology and Oceanography Bulletin*, *24*(1), 11–14. <https://doi.org/10.1002/lob.10008>
- Dugdale, R. C., Wischmeyer, A. G., Wilkerson, F. P., Barber, R. T., Chai, F., Jiang, M. S., & Peng, T. H. (2002). Meridional asymmetry of source nutrients to the equatorial Pacific upwelling ecosystem and its potential impact on ocean-atmosphere CO<sub>2</sub> flux: A data and modeling approach. *Deep Sea Research Part II*, *49*(13–14), 2513–2531. [https://doi.org/10.1016/S0967-0645\(02\)00046-2](https://doi.org/10.1016/S0967-0645(02)00046-2)
- Estrada, M., Delgado, M., Blasco, D., Latasa, M., Cabello, A. M., Benitez-Barrios, V., et al. (2016). Phytoplankton across tropical and subtropical regions of the Atlantic, Indian and Pacific Oceans. *PLoS One*, *11*(3), e0151699. <https://doi.org/10.1371/journal.pone.0151699>
- Fichot, C. G., & Benner, R. (2011). A novel method to estimate DOC concentrations from CDOM absorption coefficients in coastal waters. *Geophysical Research Letters*, *38*, L03610. <https://doi.org/10.1029/2010GL046152>
- Fiedler, P. C. (2002). The annual cycle and biological effects of the Costa Rica Dome. *Deep Sea Research Part I*, *49*(2), 321–338. [https://doi.org/10.1016/S0967-0637\(01\)00057-7](https://doi.org/10.1016/S0967-0637(01)00057-7)
- Figuerola, F. L. (2002). Bio-optical characteristics of Gerlache and Bransfield Strait waters during an Antarctic summer cruise. *Deep Sea Research Part II*, *49*(4–5), 675–691. [https://doi.org/10.1016/S0967-0645\(01\)00118-7](https://doi.org/10.1016/S0967-0645(01)00118-7)
- Fileman, E. S., White, D. A., Harmer, R. A., Aytan, U., Tarran, G. A., Smyth, T., & Atkinson, A. (2017). Stress of life at the ocean's surface: Latitudinal patterns of UV sunscreens in plankton across the Atlantic. *Progress in Oceanography*, *158*, 171–184. <https://doi.org/10.1016/j.pcean.2017.01.001>
- Gao, Y., Kaufman, Y. J., Tanre, D., Kolber, D., & Falkowski, P. G. (2001). Seasonal distributions of aeolian iron fluxes to the global ocean. *Geophysical Research Letters*, *28*(1), 29–32. <https://doi.org/10.1029/2000GL011926>

- Garcia-Corral, L. S., Holding, J. M., Carrillo-de-Albornoz, P., Steckbauer, A., Perez-Lorenzo, M., Navarro, N., et al. (2017). Effects of UVB radiation on net community production in the upper global ocean. *Global Ecology and Biogeography*, 26(1), 54–64. <https://doi.org/10.1111/geb.12513>
- Garver, S. A., Siegel, D. A., & Mitchell, B. G. (1994). Variability in near-surface particulate absorption-spectra—What can a satellite ocean color imager see? *Limnology & Oceanography*, 39(6), 1349–1367. <https://doi.org/10.4319/lo.1994.39.6.1349>
- Garzoli, S. L., & Gordon, A. L. (1996). Origins and variability of the Benguela current. *Journal of Geophysical Research*, 101(C1), 897–906. <https://doi.org/10.1029/95JC03221>
- Häder, D. P., Williamson, C. E., Wangberg, S. A., Rautio, M., Rose, K. C., Gao, K., et al. (2015). Effects of UV radiation on aquatic ecosystems and interactions with other environmental factors. *Photochemical and Photobiological Sciences*, 14(1), 108–126. <https://doi.org/10.1039/c4pp90035a>
- Hargreaves, B. R. (2003). Water column optics and penetration of UVR. In E. W. Helbling, & H. Zagarese (Eds.), *UV effects in aquatic organisms and ecosystems* (p. 59). Cambridge, UK: The Royal Society of Chemistry.
- Helms, J. R., Stubbins, A., Perdue, E. M., Green, N. W., Chen, H., & Mopper, K. (2013). Photochemical bleaching of oceanic dissolved organic matter and its effect on absorption spectral slope and fluorescence. *Marine Chemistry*, 155, 81–91. <https://doi.org/10.1016/j.marchem.2013.05.015>
- Hutchings, L., van der Lingen, C. D., Shannon, L. J., Crawford, R. J. M., Verheye, H. M. S., Bartholomae, C. H., et al. (2009). The Benguela Current: An ecosystem of four components. *Progress in Oceanography*, 83(1–4), 15–32. <https://doi.org/10.1016/j.pocan.2009.07.046>
- Iuculano, F., Alvarez-Salgado, X. A., Otero, J., Catala, T. S., Sobrino, C., Duarte, C. M., & Agusti, S. (2019). Patterns and drivers of UV absorbing chromophoric dissolved organic matter in the euphotic layer of the open ocean. *Frontiers in Marine Science*, 6, 320. <https://doi.org/10.3389/fmars.2019.00320>
- Jiang, M. S., & Chai, F. (2005). Physical and biological controls on the latitudinal asymmetry of surface nutrients and pCO<sub>2</sub> in the central and eastern equatorial Pacific. *Journal of Geophysical Research*, 110, C06007. <https://doi.org/10.1029/2004JC002715>
- Jickells, T. D., An, Z. S., Andersen, K. K., Baker, A. R., Bergametti, G., Brooks, N., et al. (2005). Global iron connections between desert dust, ocean biogeochemistry, and climate. *Science*, 308(5718), 67–71. <https://doi.org/10.1126/science.1105959>
- Kessler, W. S. (2006). The circulation of the eastern tropical Pacific: A review. *Progress in Oceanography*, 69(2–4), 181–217. <https://doi.org/10.1016/j.pocan.2006.03.009>
- Kirk, J. T. (1994). *Light and photosynthesis in aquatic ecosystems*, (p. 382). Cambridge University Press. <https://doi.org/10.1038/309382a0>
- Kitidis, V., Stubbins, A. P., Uher, G., Goddard, R. C. U., Law, C. S., & Woodward, E. M. S. (2006). Variability of chromophoric organic matter in surface waters of the Atlantic Ocean. *Deep Sea Research Part II*, 53(14–16), 1666–1684. <https://doi.org/10.1016/j.dsr2.2006.05.009>
- Kuwahara, V. S., Nakajima, R., Othman, B. H. R., Kushairi, M. R. M., & Toda, T. (2010). Spatial variability of UVR attenuation and bio-optical factors in shallow coral-reef waters of Malaysia. *Coral Reefs*, 29(3), 693–704. <https://doi.org/10.1007/s00338-010-0618-1>
- Lamont, T., Barlow, R. G., & Kyewalyanga, M. S. (2014). Physical drivers of phytoplankton production in the southern Benguela upwelling system. *Deep Sea Research Part I*, 90, 1–16. <https://doi.org/10.1016/j.dsr.2014.03.003>
- Lee, Z., Wei, J. W., Voss, K., Lewis, M., Bricaud, A., & Huot, Y. (2015). Hyperspectral absorption coefficient of “pure” seawater in the range of 350–550 nm inverted from remote sensing reflectance. *Applied Optics*, 54(3), 546–558. <https://doi.org/10.1364/Ao.54.000546>
- Lee, Z., Weidemann, A., Kindle, J., Arnone, R., Carder, K. L., & Davis, C. (2007). Euphotic zone depth: Its derivation and implication to ocean-color remote sensing. *Journal of Geophysical Research*, 112, C03009. <https://doi.org/10.1029/2006JC003802>
- Levitus, S., Conkright, M. E., Reid, J. L., Najjar, R. G., & Mantyla, A. (1993). Distribution of nitrate, phosphate and silicate in the world oceans. *Progress in Oceanography*, 31(3), 245–273. [https://doi.org/10.1016/0079-6611\(93\)90003-V](https://doi.org/10.1016/0079-6611(93)90003-V)
- Llabres, M., Agusti, S., Alonso-Laita, P., & Herndl, G. J. (2010). *Synechococcus* and *Prochlorococcus* cell death induced by UV radiation and the penetration of lethal UVR in the Mediterranean Sea. *Marine Ecology Progress Series*, 399, 27–37. <https://doi.org/10.3354/meps08332>
- Llabres, M., Agusti, S., Fernandez, M., Canepa, A., Maurin, F., Vidal, F., & Duarte, C. M. (2013). Impact of elevated UVB radiation on marine biota: A meta-analysis. *Global Ecology and Biogeography*, 22(1), 131–144. <https://doi.org/10.1111/j.1466-8238.2012.00784.x>
- Longhurst, A. R. (2010). *Ecological geography of the sea*. Elsevier Science.
- Mahowald, N. M., Baker, A. R., Bergametti, G., Brooks, N., Duce, R. A., Jickells, T. D., et al. (2005). Atmospheric global dust cycle and iron inputs to the ocean. *Global Biogeochemical Cycles*, 19, GB4025. <https://doi.org/10.1029/2004GB002402>
- Marañón, E., Fernández, A., Mouriño-Carballido, B., Martínez-García, S., Teira, E., Cermeño, P., et al. (2010). Degree of oligotrophy controls the response of microbial plankton to Saharan dust. *Limnology & Oceanography*, 55(6), 2339–2352. <https://doi.org/10.4319/lo.2010.55.6.2339>
- Michael, K. J., Veal, C. J., & Nunez, M. (2012). Attenuation coefficients of ultraviolet and photosynthetically active wavelengths in the waters of Heron Reef, Great Barrier Reef, Australia. *Marine and Freshwater Research*, 63(2), 142–149. <https://doi.org/10.1071/MF11106>
- Mitchell, B. G., Kahru, M., Wieland, J., & Stramska, M. (2003). Determination of spectral absorption coefficients of particles, dissolved material and phytoplankton for discrete water samples. In J. L. Mueller, G. S. Fargion, & C. R. McClain (Eds.), *Ocean optics protocols for satellite ocean color sensor validation, Revision 4, Volume IV: Inherent optical properties: Instruments, characterizations, field measurements and data analysis protocols* (pp. 39–64). Greenbelt, MD: NASA.
- Mitchell, B. G., & Kiefer, D. A. (1984). Determination of absorption and fluorescence excitation spectra for phytoplankton. In O. Holm-Hansen, L. Bolis, & R. Gilles (Eds.), *Marine phytoplankton and productivity: Proceedings of the invited lectures to a symposium organized within the 5th Conference of the European Society for Comparative Physiology and Biochemistry—Taormina, Sicily, Italy, September 5–8, 1983* (pp. 157–169). Berlin, Heidelberg: Springer. <https://doi.org/10.1029/ln008p0157>
- Moore, C. M., Mills, M. M., Milne, A., Langlois, R., Achterberg, E. P., Lochte, K., et al. (2006). Iron limits primary productivity during spring bloom development in the central North Atlantic. *Global Change Biology*, 12(4), 626–634. <https://doi.org/10.1111/j.1365-2486.2006.01122.x>
- Mopper, K., & Kieber, D. (2002). Photochemistry and the cycling of carbon, sulphur, nitrogen and phosphorus. In D. A. Hansell, & C. A. Carlson (Eds.), *Biogeochemistry of marine dissolved organic matter*. San Diego, CA: Academic Press.
- Morel, A., Ahn, Y. H., Partensky, F., Vaulot, D., & Claustre, H. (1993). *Prochlorococcus* and *Synechococcus*—A comparative-study of their optical-properties in relation to their size and pigmentation. *Journal of Marine Research*, 51(3), 617–649. <https://doi.org/10.1357/0022240933223963>
- Morel, A., Claustre, H., Antoine, D., & Gentili, B. (2007). Natural variability of bio-optical properties in case 1 waters: Attenuation and reflectance within the visible and near-UV spectral domains, as observed in south Pacific and Mediterranean waters. *Biogeosciences*, 4(5), 913–925. <https://doi.org/10.5194/bg-4-913-2007>
- Morel, A., Claustre, H., & Gentili, B. (2010). The most oligotrophic subtropical zones of the global ocean: Similarities and differences in terms of chlorophyll and yellow substance. *Biogeosciences*, 7(10), 3139–3151. <https://doi.org/10.5194/bg-7-3139-2010>
- Morel, A., Gentili, B., Claustre, H., Babin, M., Bricaud, A., Ras, J., & Tieche, F. (2007). Optical properties of the “clearest” natural waters. *Limnology & Oceanography*, 52(1), 217–229. <https://doi.org/10.4319/lo.2007.52.1.0217>

- Morel, A., & Maritorena, S. (2001). Bio-optical properties of oceanic waters: A reappraisal. *Journal of Geophysical Research*, 106(C4), 7163–7180. <https://doi.org/10.1029/2000JC000319>
- Morrison, J. R., & Nelson, N. B. (2004). Seasonal cycle of phytoplankton UV absorption at the Bermuda Atlantic Time-series Study (BATS) site. *Limnology & Oceanography*, 49(1), 215–224. <https://doi.org/10.4319/lo.2004.49.1.0215>
- Morrow, J., Chamberlin, W., & Kiefer, D. (1989). A two-component description of spectral absorption by marine particles. *Limnology & Oceanography*, 34(8), 1500–1509. <https://doi.org/10.4319/lo.1989.34.8.1500>
- Nelson, J. R., & Guarda, S. (1995). Particulate and dissolved spectral absorption on the continental-shelf of the Southeastern United States. *Journal of Geophysical Research*, 100(C5), 8715–8732. <https://doi.org/10.1029/95JC00222>
- Nelson, N. B., Carlson, C. A., & Steinberg, D. K. (2004). Production of chromophoric dissolved organic matter by Sargasso Sea microbes. *Marine Chemistry*, 89(1–4), 273–287. <https://doi.org/10.1016/j.marchem.2004.02.017>
- Nelson, N. B., & Siegel, D. A. (2013). The global distribution and dynamics of chromophoric dissolved organic matter. *Annual Review of Marine Science*, 5, 447–476. <https://doi.org/10.1146/annurev-marine-120710-100751>
- Nelson, N. B., Siegel, D. A., Carlson, C. A., & Swan, C. M. (2010). Tracing global biogeochemical cycles and meridional overturning circulation using chromophoric dissolved organic matter. *Geophysical Research Letters*, 37, L03610. <https://doi.org/10.1029/2009GL042325>
- Nelson, N. B., Siegel, D. A., & Michaels, A. F. (1998). Seasonal dynamics of colored dissolved material in the Sargasso Sea. *Deep Sea Research Part I*, 45(6), 931–957. [https://doi.org/10.1016/S0967-0637\(97\)00106-4](https://doi.org/10.1016/S0967-0637(97)00106-4)
- Obernosterer, I., Ruardij, P., & Herndl, G. J. (2001). Spatial and diurnal dynamics of dissolved organic matter (DOM) fluorescence and H<sub>2</sub>O<sub>2</sub> and the photochemical oxygen demand of surface water DOM across the subtropical Atlantic Ocean. *Limnology & Oceanography*, 46(3), 632–643. <https://doi.org/10.4319/lo.2001.46.3.0632>
- Organelli, E., Bricaud, A., Antoine, D., & Matsuoka, A. (2014). Seasonal dynamics of light absorption by chromophoric dissolved organic matter (CDOM) in the NW Mediterranean Sea (BOUSSOLE site). *Deep Sea Research Part I*, 91, 72–85. <https://doi.org/10.1016/j.dsr.2014.05.003>
- Overmans, S., & Agustí, S. (2019). Latitudinal gradient of UV attenuation along the highly transparent Red Sea basin. *Photochemistry and Photobiology*, 95(5), 1267–1279. <https://doi.org/10.1111/php.13112>
- Overmans, S., & Agustí, S. (2020). Unraveling the seasonality of UV exposure in reef waters of a rapidly warming (sub-)tropical sea. *Frontiers in Marine Science*, 7(111), 111. <https://doi.org/10.3389/fmars.2020.00111>
- Pabortsava, K., Lampitt, R. S., Benson, J., Crowe, C., McLachlan, R., Le Moigne, F. A. C., et al. (2017). Carbon sequestration in the deep Atlantic enhanced by Saharan dust. *Nature Geoscience*, 10(3), 189–194. <https://doi.org/10.1038/Ngeo2899>
- Paul, N. D., & Gwynn-Jones, D. (2003). Ecological roles of solar UV radiation: Towards an integrated approach. *Trends in Ecology & Evolution*, 18(1), 48–55. [https://doi.org/10.1016/S0169-5347\(02\)00014-9](https://doi.org/10.1016/S0169-5347(02)00014-9)
- Pérez-Hernández, M., Nuez-de-la-Fuente, M., Vélez-Belchí, P., Benítez-Barríos, V. M., López-Laatzén, F., & Fraile-Nuez, E. (2012). Análisis de muestras de salinidad. Salinómetro de laboratorio Autosal 8400B. In E. Moreno-Ostos (Ed.), *Expedición de Circumnavegación Malaspina 2010: Cambio Global y Exploración de la Biodiversidad del Océano. Libro Blanco de Métodos y Técnicas de Trabajo Oceanográfico* (pp. 67–76). Madrid: CSIC.
- Piazena, H., Perez-Rodriguez, E., Hader, D. P., & Lopez-Figueroa, F. (2002). Penetration of solar radiation into the water column of the central subtropical Atlantic Ocean—Optical properties and possible biological consequences. *Deep Sea Research Part II*, 49(17), 3513–3528. [https://doi.org/10.1016/S0967-0645\(02\)00093-0](https://doi.org/10.1016/S0967-0645(02)00093-0)
- Pinedo-González, P., West, A. J., Tovar-Sánchez, A., Duarte, C. M., Maraño, E., Cermeño, P., et al. (2015). Surface distribution of dissolved trace metals in the oligotrophic ocean and their influence on phytoplankton biomass and productivity. *Global Biogeochemical Cycles*, 29, 1763–1781. <https://doi.org/10.1002/2015GB005149>
- Quintero-Torres, R., Aragon, J. L., Torres, M., Estrada, M., & Cros, L. (2006). Strong far-field coherent scattering of ultraviolet radiation by holococcolithophores. *Physical Review E*, 74(3 Pt 1), 032901. <https://doi.org/10.1103/PhysRevE.74.032901>
- Rasmus, K. E., Graneli, W., & Wangberg, S. A. (2004). Optical studies in the Southern Ocean. *Deep Sea Research Part II*, 51(22–24), 2583–2597. <https://doi.org/10.1016/j.dsr2.2001.01.004>
- Reynolds, R. A., Stramski, D., & Mitchell, B. G. (2001). A chlorophyll-dependent semianalytical reflectance model derived from field measurements of absorption and backscattering coefficients within the Southern Ocean. *Journal of Geophysical Research*, 106(C4), 7125–7138. <https://doi.org/10.1029/1999JC000311>
- Sempere, R., Para, J., Tedetti, M., Charriere, B., & Mallet, M. (2015). Variability of solar radiation and CDOM in surface coastal waters of the Northwestern Mediterranean Sea. *Photochemistry and Photobiology*, 91(4), 851–861. <https://doi.org/10.1111/php.12434>
- Smith, R. C., Prezelin, B. B., Baker, K. S., Bidigare, R. R., Boucher, N. P., Coley, T., et al. (1992). Ozone depletion: Ultraviolet radiation and phytoplankton biology in Antarctic waters. *Science*, 255(5047), 952–959. <https://doi.org/10.1126/science.1546292>
- Smyth, T. J. (2011). Penetration of UV irradiance into the global ocean. *Journal of Geophysical Research*, 116, C11020. <https://doi.org/10.1029/2011JC007183>
- Stamler, N., Lovengreen, C., & Tilzer, M. M. (1997). The underwater light field in the Bellingshausen and Amundsen seas (Antarctica). *Hydrobiologia*, 344, 41–56. <https://doi.org/10.1023/A:1002993925441>
- Stramski, D., Babin, M., & Wozniak, S. B. (2007). Variations in the optical properties of terrigenous mineral-rich particulate matter suspended in seawater. *Limnology & Oceanography*, 52(6), 2418–2433. <https://doi.org/10.4319/lo.2007.52.6.2418>
- Stramski, D., Boss, E., Bogucki, D., & Voss, K. J. (2004). The role of seawater constituents in light backscattering in the ocean. *Progress in Oceanography*, 61(1), 27–56. <https://doi.org/10.1016/j.pocean.2004.07.001>
- Swan, C. M., Siegel, D. A., Nelson, N. B., Carlson, C. A., & Nasir, E. (2009). Biogeochemical and hydrographic controls on chromophoric dissolved organic matter distribution in the Pacific Ocean. *Deep Sea Research Part I*, 56(12), 2175–2192. <https://doi.org/10.1016/j.dsr.2009.09.002>
- Tedetti, M., & Sempere, R. (2006). Penetration of ultraviolet radiation in the marine environment: A review. *Photochemistry and Photobiology*, 82(2), 389–397. <https://doi.org/10.1562/2005-11-09-IR-733>
- Tedetti, M., Sempere, R., Vasilkov, A., Charriere, B., Nerini, D., Miller, W. L., et al. (2007). High penetration of ultraviolet radiation in the south east Pacific waters. *Geophysical Research Letters*, 34, L12610. <https://doi.org/10.1029/2007GL029823>
- Twardowski, M. S., & Donaghay, P. L. (2001). Separating in situ and terrigenous sources of absorption by dissolved materials in coastal waters. *Journal of Geophysical Research*, 106(C2), 2545–2560. <https://doi.org/10.1029/1999JC000039>
- Vaillancourt, R. D., Brown, C. W., Guillard, R. R. L., & Balch, W. M. (2004). Light backscattering properties of marine phytoplankton: Relationships to cell size, chemical composition and taxonomy. *Journal of Plankton Research*, 26(2), 191–212. <https://doi.org/10.1093/plankt/fbh012>
- Vasilkov, A. P., Herman, J. R., Ahmad, Z., Kahru, M., & Mitchell, B. G. (2005). Assessment of the ultraviolet radiation field in ocean waters from space-based measurements and full radiative-transfer calculations. *Applied Optics*, 44(14), 2863–2869. <https://doi.org/10.1364/ao.44.002863>
- Wang, X. J., Murtugudde, R., Hackert, E., & Maraño, E. (2013). Phytoplankton carbon and chlorophyll distributions in the equatorial Pacific and Atlantic: A basin-scale comparative study. *Journal of Marine Systems*, 109, 138–148. <https://doi.org/10.1016/j.jmarsys.2012.03.004>

- Weatherhead, E. C., & Andersen, S. B. (2006). The search for signs of recovery of the ozone layer. *Nature*, *441*(7089), 39–45. <https://doi.org/10.1038/nature04746>
- Weinbauer, M. G., Wilhelm, S. W., Suttle, C. A., & Garza, D. R. (1997). Photoreactivation compensates for UV damage and restores infectivity to natural marine virus communities. *Applied and Environmental Microbiology*, *63*(6), 2200–2205. <https://doi.org/10.1128/AEM.63.6.2200-2205.1997>